Bull Volcanol (2006) 68: 567–591
DOI 10.1007/s00445-005-0033-6

RESEARCH ARTICLE

Carmela Freda · Mario Gaeta · Daniel B. Karner · Fabrizio Marra · Paul R. Renne · Jacopo Taddeucci · Piergiorgio Scarlato · John N. Christensen · Luigi Dallai

Eruptive history and petrologic evolution of the Albano multiple maar (Alban Hills, Central Italy)

Received: 16 September 2004 / Accepted: 29 August 2005 / Published online: 25 February 2006

Abstract A comprehensive volcanological study of the Albano multiple maar (Alban Hills, Italy) using (i) $^{40}Ar/^{39}Ar$ geochronology of the most complete stratigraphic section and other proximal and distal outcrops and (ii) petrographic observations, phase analyses of major and trace elements, and Sr and O isotopic analyses of the pyroclastic deposits shows that volcanic activity at Albano was strongly discontinuous, with a first eruptive cycle at 69±1 ka producing at least two eruptions, and a second cycle with two peaks at 39±1 and 36±1 ka producing at least four eruptions. Contrary to previous studies, we did not find evidence of magmatic or hydromagmatic eruptions younger than 36±1 ka. The activity of Albano was fed by a new batch of primary magma compositionally different from that of the older activity of the Alban Hills; moreover, the REE and $^{87}Sr/^{86}Sr$ data indicate that the Albano magma originated from an enriched metasomatized mantle. According to the modeled liquid line of descent, this magma differentiated under the influence of magma/limestone wall rock interaction. Our detailed eruptive and petrologic reconstruction of the Albano Maar evolution substantiates the dormant state of the Alban Hills Volcanic District.

Keywords Eruptive cycles · Geochronology · Alban Hills · Maar · Hydromagmatic · Ultrapotassic · Decarbonation

Electronic Supplementary Material Supplementary material is available for this article at http://dx.doi.org/10.1007/s00445-005-0033-6

Editorial responsibility: J. Donnelly-Nolan

C. Freda (✉) · F. Marra · J. Taddeucci · P. Scarlato
Istituto Nazionale di Geofisica e Vulcanologia, Sezione di Sismologia e Tettonofisica,
Via di Vigna Murata,
605-00143 Roma, Italy
e-mail: freda@ingv.it
Tel.: +39-06-51860502
Fax: +39-06-51860507

M. Gaeta
Dipartimento di Scienze della Terra, Università degli Studi "La Sapienza",
P. Aldo Moro,
5-00185 Roma, Italy

D. B. Karner
Dept of Geology, Sonoma State University,
1801 East Cotati Ave., Rohnert Park, CA 94928, USA

P. R. Renne
Berkeley Geochronology Center,
2455 Ridge Road, Berkeley, CA 94709, USA

P. R. Renne
Dept of Earth and Planetary Science, University of California,
Berkeley, CA 94720, USA

J. N. Christensen
Lawrence Berkeley National Laboratory,
1 Cyclotron Road, MS 70A4418 Berkeley, CA 94720, USA

L. Dallai
CNR-Istituto di Geologia Ambientale e Geoingegneria,
Via Bolognola,
7-00138 Rome, Italy

Introduction

The Alban Hills is one of the main volcanic districts of the potassic and ultrapotassic magmatic province that developed along the Tyrrhenian margin of Italy during middle and late Pleistocene time (Marra et al. 2004 and references therein). This magmatism, generated in a very complex tectonic setting (Doglioni et al. 1999), is thought to result from the combined effect of source metasomatism, crystal fractionation, and crustal assimilation (Conticelli et al. 2002 and references therein). The volcanic products from the Alban Hills are included in the high-K magma series (HKS, Peccerillo and Manetti 1985) and are characterized by a narrow SiO_2 and alkali range (Trigila et al. 1995), high LREE/HREE ratio (Peccerillo et al. 1984), very constant $^{87}Sr/^{86}Sr$ initial ratio (Ferrara et al. 1985) and plagioclase-free paragenesis (Palladino et al. 2001). On the basis of these geochemical features, the Alban Hills magmas were generally interpreted to be primitive magmas (Ferrara et al. 1985). Difficulties in understanding the petrological

evolution of the Alban Hills magmas were due to the unusual silica depletion of residual melts (Trigila et al. 1995) and to the lack of glass-bearing juvenile (lava and scoria clast) volcanic rocks, with an exception being the fiamme in the Villa Senni Lower Flow Unit (Freda et al. 1997).

The Albano multiple maar (Fig. 1) hosted the most recent activity of the Alban Hills Volcanic District (Villa et al. 1999; Karner et al. 2001a; Marra et al. 2003; Funiciello et al. 2002; Funiciello et al. 2003). Recent papers (Karner et al. 2001b; Marra et al. 2003) propose that the activity of Albano is possibly a new phase of volcanic activity from the Alban Hills Volcanic District. This differs from previous interpretations that considered the Albano activity to be the final hydromagmatic stage, following the Monte delle Faete strombolian-effusive phase and the Tuscolano-Artemisio main explosive, ignimbrite-forming phase (De Rita et al. 1988; De Rita et al. 1995a). Knowing whether the Alban Hills is an extinct volcanic centre or is undergoing a resurgence in activity is of central importance to the assessment of potential volcanic hazards for the city of Rome.

Using a multidisciplinary approach, we investigate the eruptive history and geochemical characteristics of the Albano Maar. This project was facilitated by the fact that the Albano pyroclastic deposits, unlike the older Alban Hills volcanic rocks, commonly consist of glass-bearing juvenile products that enable the characterization of the melt phase and the definition of its petrological evolution. The most complete stratigraphic section and some near and distal outcrops of the Albano products have been studied using $^{40}Ar/^{39}Ar$ geochronology, petrographic observations, phase microprobe analyses, and Sr and O isotopic analyses. We use glass compositions and the chemical variability of clinopyroxene as a differentiation index for these magmas. In particular, we combine strontium and oxygen isotope and rare earth element (REE) data from clinopyroxenes to constrain mantle and crustal contributions to the Albano magma source. Our goal is to develop a detailed chronology of the eruptive events and to investigate the petrological evolution of the Albano Maar in order to define its volcanic and magmatic history and assess future volcanic hazards.

Stratigraphy

The first attempt to map the different eruptive units of the Albano Maar was made by De Rita et al. (1988) in a 1:50000 scale geologic map of the Alban Hills. De Rita et al. (1988) recognized seven stratigraphic units, comprising four hydromagmatic deposits, one pyroclastic flow deposit, and two wet pyroclastic flow deposits. Later, a description of the volcanic stratigraphy with a generalized stratigraphic column was proposed (De Rita et al. 1995a, b). In these papers, the Albano Maar is described as "a multiple tuff ring, the activity of which consisted of five main explosive cycles each producing a new crater. The fifth eruption cycle of Albano emplaced a wet pyroclastic flow from the SE sector where the Albano lake shows its maximum depth". This wet pyroclastic flow is the most famous deposit from Albano, as it was quarried since the IV Century B.C. under the name of *Lapis Albanus*. The dark-grey color and the granular texture of this rock led to the local name of "peperino" (black pepper-like), and so this unit is known in the literature also as "Peperino di Marino" or "Peperino Albano". Giordano et al. (2002) define it as a phreatomagmatic ignimbrite, basic in composition, describe its stratigraphy and propose a mechanism for its emplacement.

Maar deposits typically display sharp lateral facies variations over relatively short distances, and Albano fits this description. In addition, multiple eruptions from the maar increase this lateral variability and lead to complex volcanic stratigraphy. Here we describe in detail a well-exposed (and the most complete found to date) stratigraphic section of the Albano Maar (Fig. 2). This section provides a stratigraphic reference for correlation with several others along the crater rim, as well as distal outcrops (Fig. 3).

Proximal sections

The best exposed section, within the northern crater rim of Albano (site 1 in Figs. 1 and 3, Reference section of Fig. 2), is an 80-meter-thick succession of pyroclastic deposits already described by Civitelli et al. (1975). This succession rests above a ~1.5-m-thick mature paleosol developed on pre-Albano hydromagmatic deposits attributed to the activity of the nearby Ariccia maar (203±1 ka, Marra et al. 2003). Below, pyroclastic fall deposits (250±1 ka) and lava flows (267±1 ka) of the Monte delle Faete Phase crop out (Marra et al. 2003).

Evidence of stratigraphic breaks within the Albano succession includes: (i) light brown to tawny pedogenised ash levels, usually centimeter- and rarely decimeter-thick, occasionally including plant molds; (ii) high-angle, laterally discontinuous, cross-laminated levels, attaining some centimeter in thickness, and rare, massive, chaotic, laterally discontinuous, decimeter-thick deposits, both interpreted as deposited by secondary surface processes; and (iii) angular unconformities between pyroclastic deposits, ranging in outcrop scale from centimeter- to decameter-long. All these three types of evidence can be used to divide the products of Albano into six informal units that can be correlated with the five cycles described by De Rita et al. (1995b). The Reference section displays all the lithological facies typical of maar volcanoes, the most common being wet and dry surge deposits. Towards the base of the succession, these include loose, low-angle cross-beds with lenses of lithic fragments; the central part of the succession is dominated by inversely graded, loose to very well indurated, plane-parallel beds commonly rich in accretionary lapilli; upwards in the succession, the surge deposits tend to be coarser-grained with less-evident bedding and lamination. Coarse breccia levels range from matrix-supported, lithic-rich zones within laminated ash levels to well-defined, matrix-poor beds. Millimeter- to decimeter-thick ash- and lapilli-fall levels, commonly variably graded, are abundant throughout the succession and represent preferential deposits for sampling juvenile material. Subunit b-2 (Fig. 2), occurring at the base of the second informal

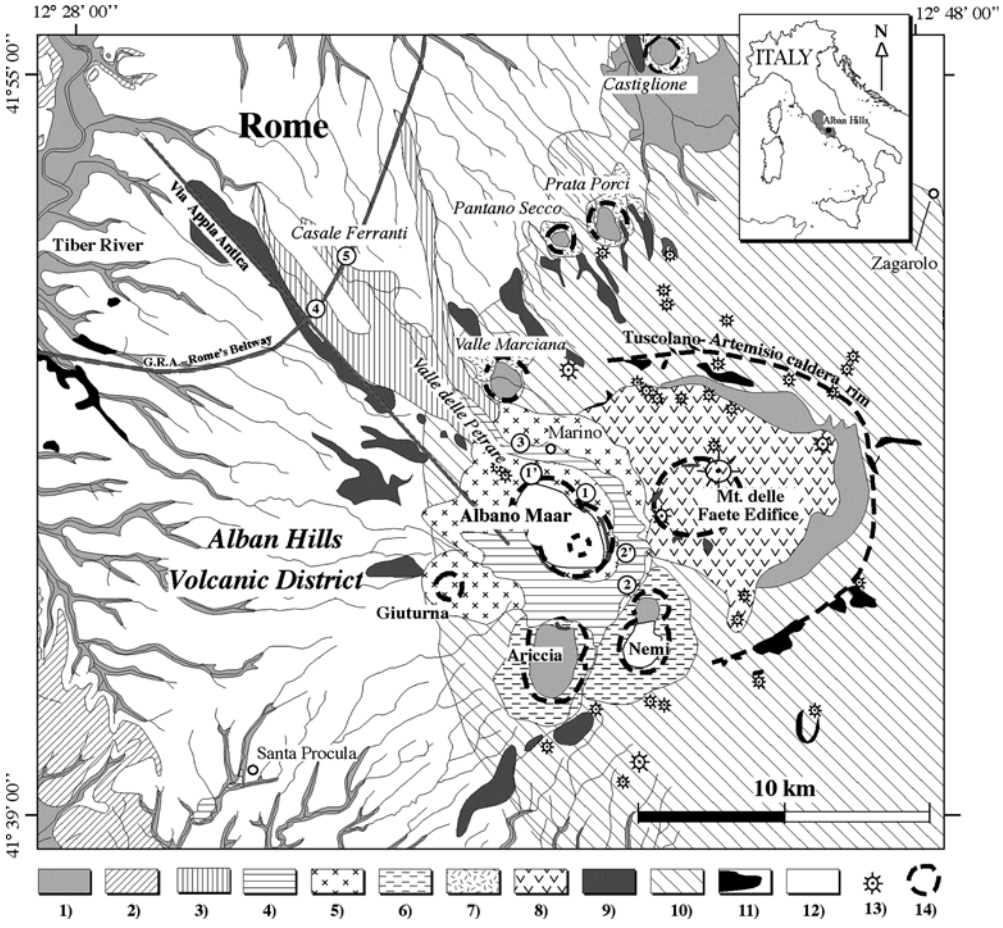

Fig. 1 Alban Hills geologic sketch and location of studied sections (*number in circles*). Legend: (1) Holocene alluvial deposit; (2) Pliocene-Quaternary sedimentary deposits; (3) Distal and partially reworked products of the hydromagmatic activity of Albano Maar (36–69 ka); (4) Peperino Albano pyroclastic-flow deposit (36 ka); (5) Hydromagmatic deposits of Albano Maar (39–69 ka); (6) Hydromagmatic deposits of Ariccia and Nemi maars (150–200 ka); (7) Hydromagmatic deposits of Monte delle Faete Phase (250–308 ka); (8) Scoria-fall deposit of Monte delle Faete Phase (250–308 ka); (9) Lava flows of Monte delle Faete Phase (270–308 ka); (10) Scoria- and Ash-fall deposit of the last stages of the Tuscolano-Artemisio Phase (351–356 ka); (11) Lava flows of the Tuscolano-Artemisio Phase (351–460 ka); (12) Pyroclastic-flow deposits of the Tuscolano-Artemisio Phase (368–561 ka); (13) Scoria cone; (14) Crater rim

unit around 27 m above the base of the succession, shows peculiar features. It is a well-lithified, almost lava-like, dark grey deposit of repeated cm- to dm-thick, plane-parallel beds of indurated ash matrix enclosing poorly vesiculated, rounded, dark scoria clasts (up to 1 cm in size), lava fragments, and sparse accretionary lapilli. A pyroclastic fall level (Subunit d-2), rich in phlogopite crystals and lithic clasts, represents the only clear stratigraphic marker for the upper part of the succession and can be traced along the northern crater rim (sites 1 and 1′ in Figs. 1 and 3). In addition to the above facies, lithified, massive, matrix-supported deposits with abundant lithic blocks crop out in paleochannels that cut through the section (Fig. 2a, Unit f).

The uppermost part of the succession is exposed in several outcrops on the eastern and southern outer rims of the Albano Maar (site 2 and 2′ in Figs. 1, 2b, and 3) where thick, lithified, massive deposits are most common. Here a loose ash- and lapilli-bearing deposit with meter-scale, low angle, cross-beds and lithic clast levels crops out. This deposit grades upward into a massive, lithified unit that we correlate to the Peperino Albano. Notably, this unit includes well-vesiculated, mm- to cm-sized pumiceous clasts. Vesiculated scoria clasts with juvenile glass (like sample AH-3C16/4Fb, site 2 in Figs. 1, 2, and 3) are quite unusual in the Alban Hills products. The only other occurrence found in the Albano sequence so far is a sparse, cm-sized-pumice horizon at the base of Subunit d-1 in the Reference section. A mention of the presence of cm-sized yellow pumice in a deposit attributed to the Albano activity is also reported in Funiciello et al. (2002). In the same area a yellow, inversely graded pumice lapilli fall layer is intercalated in the lower portion of the deposit correlated to Peperino Albano; sparse, dm-scale vesicular scoria clasts with cm-sized leucite crystals also crop out within the southeastern rim of the Albano Crater, although their stratigraphic position is uncertain.

The NW-striking Valle delle Petrare (site 3 in Figs. 1 and 3) descends from the north-western slope of the Albano crater rim, flanking the town of Marino. This is the location of the ancient Roman quarries, and can be considered the type locality of the Peperino Albano. The deposit is a grey, lithified, mostly massive ash deposit rich in polygenetic lithic blocks.

Distal sections

Distal facies of pyroclastic deposits or their reworked equivalents crop out mostly in paleovalleys. At the GRA/Appia Antica section (site 4 in Figs. 1, 2b, and 3) distal and reworked products of Albano fill a paleo-channel within fluvial-lacustrine deposits and ancient Tuscolano-Artemisio Phase pyroclastic rocks. Here, two paleosols occur within a succession of volcaniclastic deposits and were used to divide this succession into three informal units. The

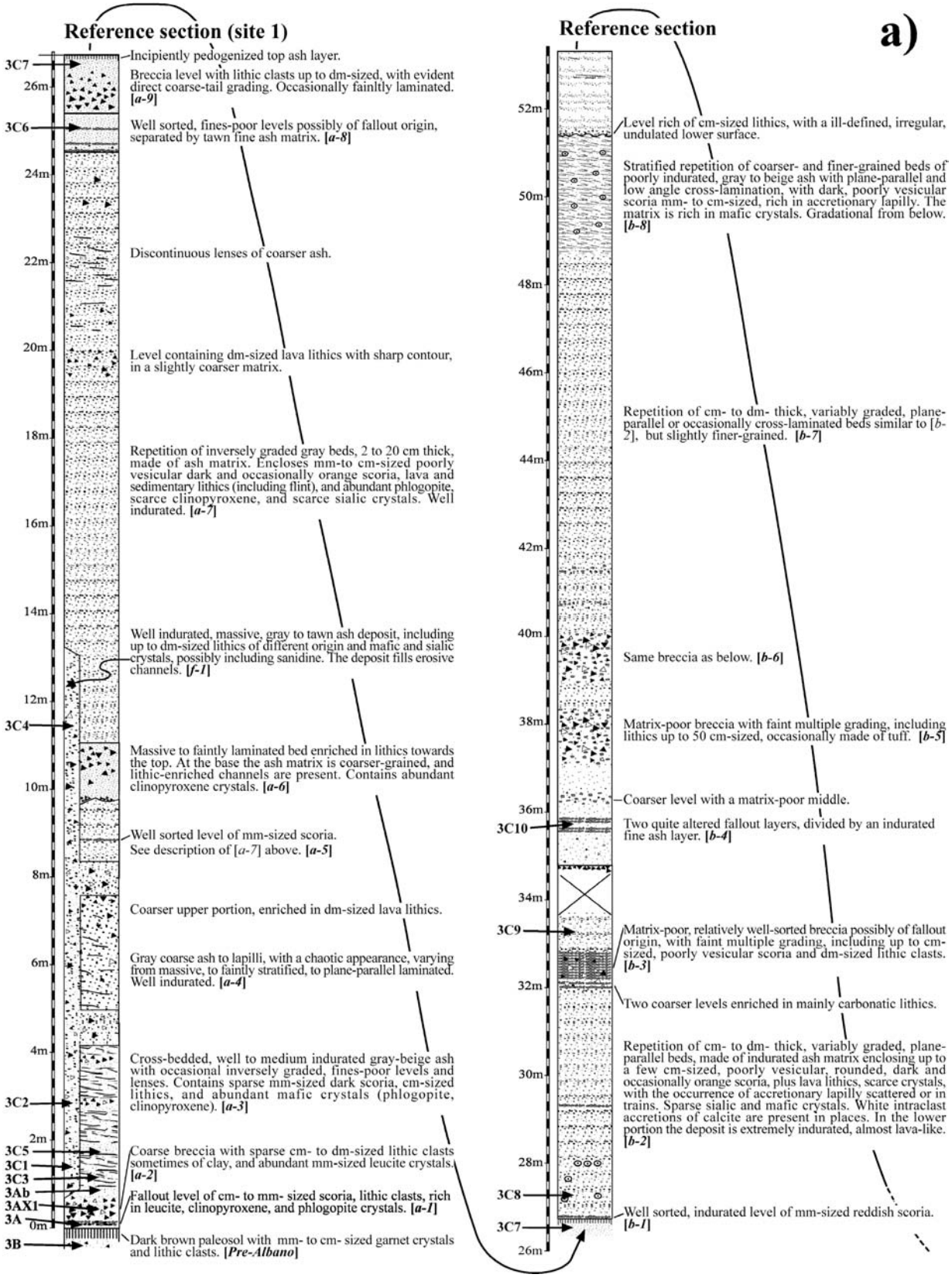

Fig. 2 Stratigraphic column and description of the investigated sections (locations are in Fig. 1). *Lower-case letters in bold italic*, indicate different units; *numbers* indicate subunits. Bold labels on the left of the column are sample labels; note that in this figure we omitted the prefix "AH-" in the sample labels

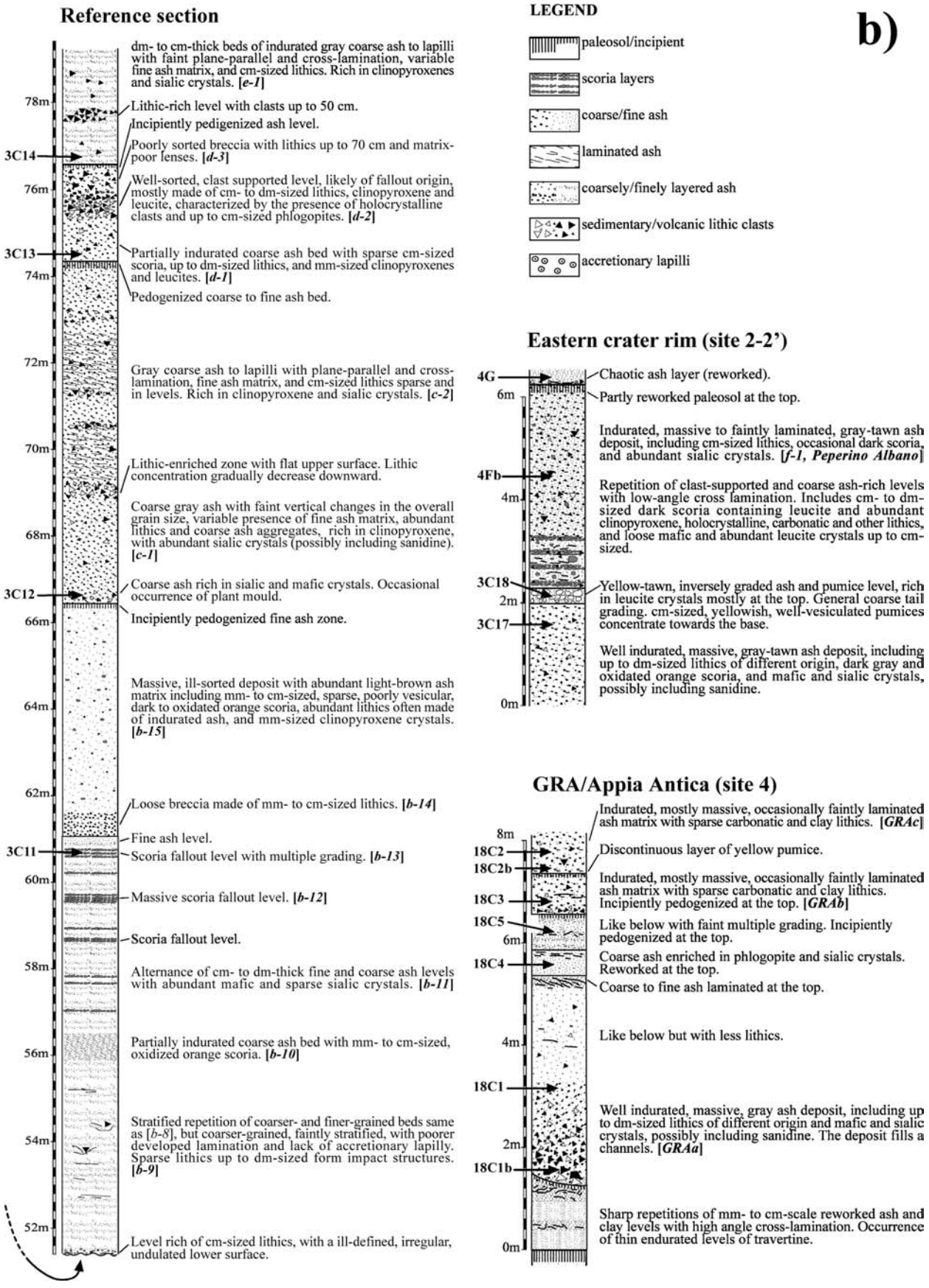

Fig. 2 Continued.

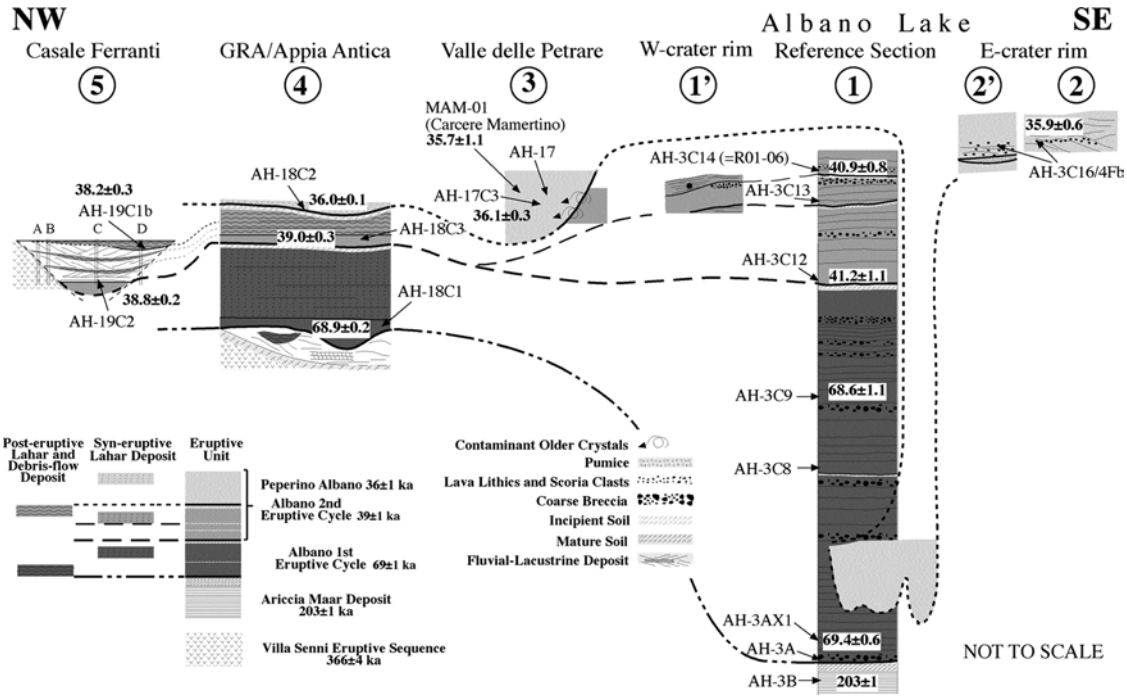

Fig. 3 Geochronology and stratigraphic correlation of the investigated sections (locations are in Fig. 1). Numbers in bold refer to the sample ages, please note that we omitted "ka"

lower, thickest unit (GRAa) includes a well-indurated, massive grey ash deposit, in places similar to Subunit b-2, grading upward into laminated, coarse- to fine-ash deposits. The middle (GRAb) and upper (GRAc) units are both indurated, mostly massive and rarely faintly laminated ash deposits. Analysis of four bore cores indicates that a similar succession fills a paleovalley at Casale Ferranti (site 5 in Figs. 1 and 3), nearby the Lucrezia Romana site of Funiciello et al. (2002).

Geochronology

Fourteen samples from the Albano Maar were dated by $^{40}Ar/^{39}Ar$ methods. When possible, leucite crystals were picked from poorly vesiculated scoria fragments, which we interpret to represent juvenile constituents of each deposit. In a few cases, leucite crystals were not obtainable from these scoria clasts, and so age analyses were performed on individual leucites selected from the ash matrix. Five to 20 single- or multiple-crystal age determinations were performed for each sample (the number of crystals used for each age determination is listed in Appendix A). Sample AH-3C12 is the only one that had a significant amount of sanidine crystals along with leucite. Sanidine crystals were separately dated, yielding an age of 45.0±2.4 ka (1σ), which is in agreement with the 41.2±1.1 ka (1σ) of leucite from the same sample (at 2σ these ages are indistinguishable). Appendix A contains the full set of $^{40}Ar/^{39}Ar$ data and in Appendix B we report details of the dating method.

The location and stratigraphic positions of the dated samples are shown in Figs. 1 and 3. The samples were selected for dating based on their position above stratigraphic discontinuities (to assess the age of the first eruption after a hiatus), or at the top of volcanic successions (in order to date the youngest eruption of Albano). Three samples (AH-3C9, AH-3C12, and AH-3C14), along with a previous age determination of a sample at the base of the succession (AH-3A, Marra et al. 2003), constrain the chronology of the Reference section. We also dated one sample at the top of the eastern crater rim (AH-3C16/4Fb) and one of Peperino Albano (AH-17C3) from the Valle delle Petrare quarries. Additional dated samples are from three layers from the distal section of GRA/Appia Antica (AH-18C1, AH18-C2, AH-18C3). Two ages were determined on the stratigraphically lowest and highest horizons within the paleovalley at Casale Ferranti (AH-19C2, AH-19C1b). Finally, we place into stratigraphic context two samples whose ages were determined in previous work: AH-9 (Santa Procula, Fig. 1) from Marra et al. (2003) and MAM-01 (site 3, Fig. 3), from Karner et al. (2001c). The age data from the earlier work were re-reduced along with the new data reported in this paper to ensure that the same assessment criteria were employed during data reduction.

Ages reported in this paper range from 36 to 69 ka and cluster around several peaks (Fig. 4) indicating that the activity occurred in discrete eruptive cycles (or epochs *sensu* Fisher and Schmincke 1984). We used the age of the stratigraphically identified eruptive units in order to better define the number, age, and rank of the cycles that occurred from the Albano Maar. The small number of age analyses obtained for each sample do not fully reflect the complete

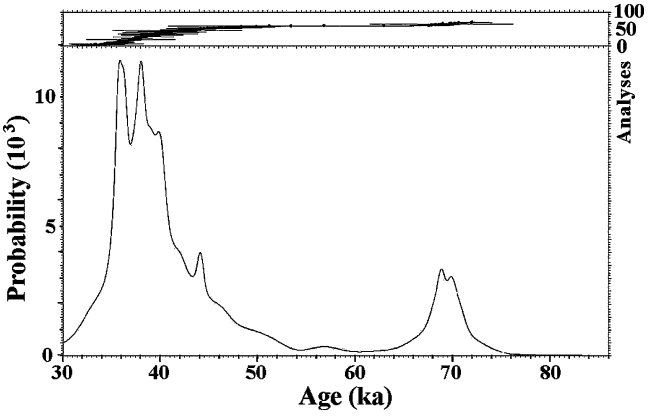

Fig. 4 Ideogram (age probability diagram) of all data included in this paper, using 2σ error distributions. Note that the small peak at 44 ka is dominated by measurement of one single crystal and its significance is negligible

Gaussian distribution of ages for that sample. Hence, it is possible that accepted techniques for assessing the eruption age for each sample (see Renne et al. 1996) by eliminating data that are not consistent with the error-weighted mean $^{40}Ar^*/^{39}Ar$ ratio at 95% confidence (2 standard deviations) can lead to erroneous interpretations about the true eruption ages. In other words, some data from each sample could represent outliers of a Gaussian distribution, and so eliminating those data could lead to a calculated eruption age for each sample that is not centered on the median value of the true sample age population. Consequently, the reported eruption age, following data elimination as per Renne et al. (1996), could lead to underestimated age uncertainty by elimination of good data. Here we have chosen not to eliminate data to make each sample internally consistent at two standard deviations. Instead, we have merged all age data from samples suspected of being from the same eruptive cycle into a single population. By doing so, we have increased the size of the sample population, so that outlier data could be eliminated with greater confidence. We plot all the data collected in this experiment, minus the obvious xenocrysts (those whose ages are in excess of 100 ka), in a single age-probability diagram (ideogram) to see how the data are distributed (Fig. 4). The ideogram contains several prominent peaks at approximately 36, 39, and 69 ka. Ages from each sample (i.e., each stratigraphic unit) tend to concentrate into the same peak of the ideogram. Based on this observation, our working hypothesis is that there are two major eruptive cycles from the Albano Maar, the second being divided in at least two sub-cycles. Field evidence (i.e., intervening soils between units, Figs. 2 and 3) shows that each cycle and sub-cycle include multiple eruptive events. However, their ages are indistinguishable with the present data set.

Based on the ideogram distributions, we have divided the age data into three subgroups (Table 1). Ideograms and inverse isochrons of each subgroup are shown in Fig. 5, without eliminating any outlying data (Fig. 5a, b, e, f, i, j) and then using "dual elimination" (Fig. 5c, d, g, h, k, l; see Vasconcelos et al. 1994) and setting the mean square weighted deviation (hereafter MSWD) threshold to 1.5 (about 90% probability of the remaining ages to be a single population). Dual elimination omits those data that contribute most to the MSWD. This MSWD threshold value was arbitrarily set, but allows for a reasonable amount of data scatter to be included in our final age calculation. Note that a more stringent MSWD of 1.0 does not change the final age calculated for each eruptive cycle or sub-cycle, nor our conclusion as to the number of eruption cycles.

The youngest population of ages, consisting of four different samples, is shown in Fig. 5a–d (see Table 1 for samples included in this population). Prior to using dual elimination, the ideogram (Fig. 5a) has positive skewness, indicating the possible inclusion of some slightly older xenocrysts, or possibly some very minor and non-uniform concentration of excess ^{40}Ar (see $^{40}Ar/^{36}Ar$ intercept in the inverse isochron of Fig. 5b; the $^{40}Ar/^{36}Ar$ air intercept is taken to be 295.5). The high MSWD (9.4) for this population (n=49) indicates that this population is not uniform, and so we have employed dual elimination to reduce the MSWD to more reasonable levels (MSWD threshold set to 1.5). Fig. 5c is the ideogram following dual elimination. The ideogram now has a nearly symmetrical peak, with MSWD of 1.4, for a population of n=38. The symmetric peak of the ideogram is caused in part by our decision to use dual elimination. Nonetheless, the inverse isochron for these data (Fig. 5d) yield an age that is identical to that in Fig. 5b, and the $^{40}Ar/^{36}Ar$ intercept (299.9±1.6, 1σ) is now nearly consistent with air (295.5). However, considering that it is possible that this sample contains a small component of excess ^{40}Ar, we interpret the inverse isochron age, which corrects for non-atmospheric initial $^{40}Ar/^{36}Ar$ ratio, to be the eruption age of this unit. Based on this analysis of the data, and the insensitivity of the final age to the elimination of data based on a smaller MSWD threshold, we conclude that the youngest eruptive sub-cycle from the Albano Maar is 36±1 ka (2σ).

The second youngest population of ages contains data from seven different samples (see Table 1 for list). Figure 5e shows the ideogram of these data prior to dual elimination. The ideogram is positively skewed, indicating the possible inclusion of some slightly older xenocrysts, or possibly some non-uniform concentration of excess ^{40}Ar (see $^{40}Ar/^{36}Ar$ intercept of 305.2±1.3 in the inverse isochron of Fig. 5f). The high MSWD (13) for this population (n=37) indicates that it is not uniform, and so we have employed dual elimination to reduce the MSWD to more reasonable levels (MSWD threshold set to 1.5). Figure 5g is the ideogram following dual elimination. The ideogram continues to have a slightly asymmetric peak. The inverse isochron for these data (Fig. 5h) yields an age of 39±1 ka (2σ), but the $^{40}Ar/^{36}Ar$ intercept (303.2±1.4) continues to be inconsistent with air (295.5). Because of this non-air intercept, we interpret the inverse isochron age, which corrects for the potential excess ^{40}Ar, to be the eruption age of this cycle. Based on this analysis of the data, we interpret that an eruptive sub-cycle occurred at 39±1 ka (2σ), and it

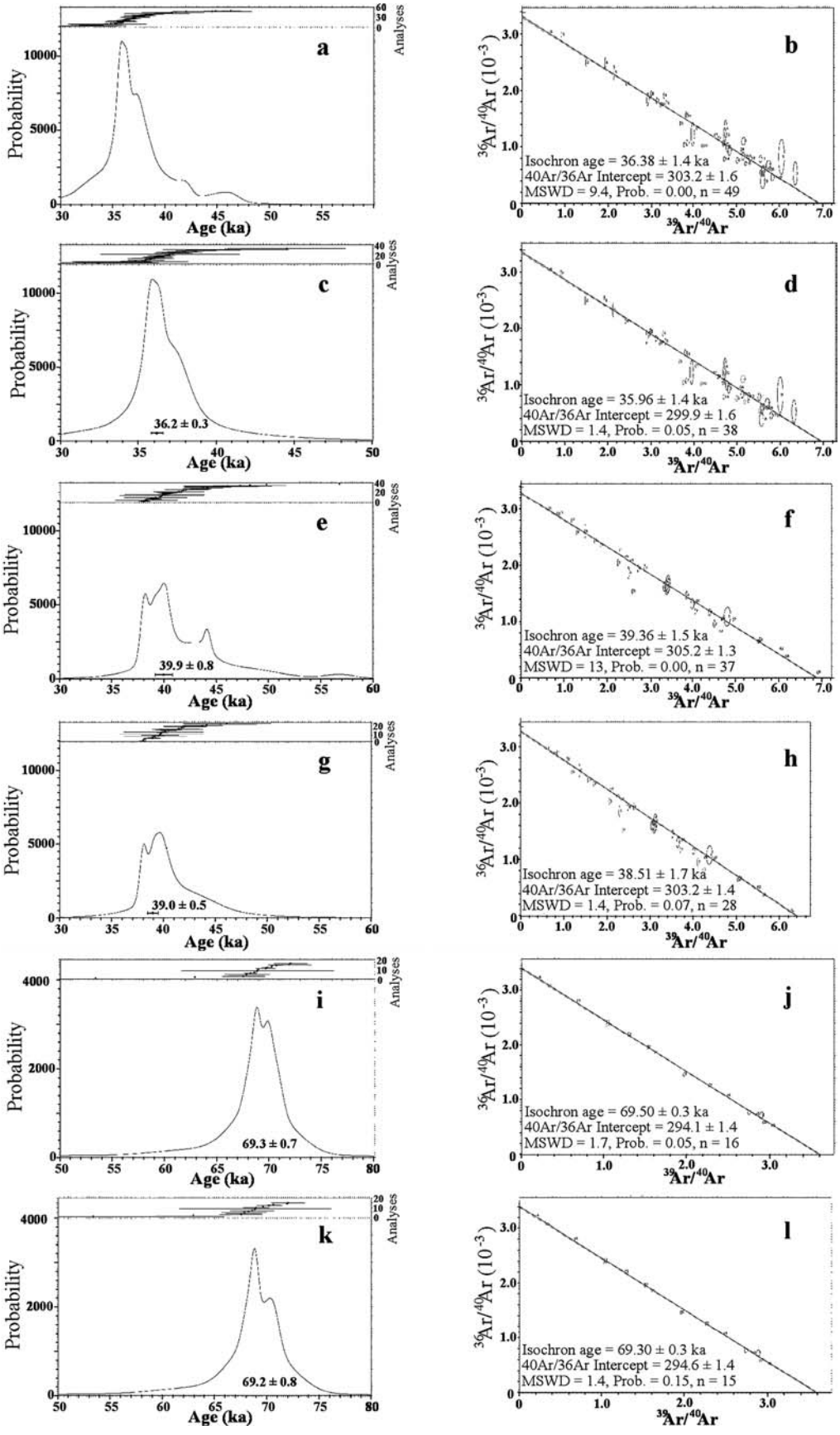

Fig. 5 (**a**) Ideogram of youngest population of samples, no data elimination, using 2σ error distributions. (**b**) Inverse isochron of data in youngest population, no elimination, using 2σ error distributions. (**c**) Ideogram of youngest population following dual elimination to reduce MSWD to below 1.5, using 2σ error distributions. (**d**) Inverse isochron of data in youngest population following dual elimination, using 2σ error distributions. (**e**) Ideogram of data from second youngest population, no elimination, using 2σ error distributions. (**f**) Inverse isochron of second youngest population, no elimination, using 2σ error distributions. (**g**) Ideogram of second youngest population, dual elimination, using 2σ error distributions. (**h**) Inverse isochron of second youngest population, dual elimination, using 2σ error distributions. (**i**) Ideogram of oldest population, no elimination, using 2σ error distributions. (**j**) Inverse isochron of oldest population, no elimination, using 2σ error distributions. (**k**). Ideogram of oldest population, dual elimination, using 2σ error distributions. (**l**) Inverse isochron of oldest population, dual elimination, using 2σ error distributions

Table 1 $^{40}Ar/^{39}Ar$ age. The sample location (site) is shown in Fig. 1. See the text for Carcere Mamertino location

Sample	Site	Latitude	Longitude	Age (ka)	±1σ
Samples included in the youngest population					
AH-3C16/4Fb	2-2′	41°44′34.24″	12°42′12.84″	35.9	0.6
AH-18C2	4	41°48′34.05″	12°34′08.09″	36.0	0.1
MAM-01	Carcere Mamertino	41°53′33.98″	12°28′58.58″	35.7	1.1
AH-17C3	3	41°46′14.59″	12°38′30.62″	36.1	0.3
Samples included in the 2nd youngest population					
AH-19C1b	5	41°39′43.78″	12°34′48.83″	38.2	0.3
AH-19C2	5	41°39′43.78″	12°34′48.83″	38.8	0.2
AH-18C3	4	41°48′34.05″	12°34′08.09″	39.0	0.3
AH-3C14	1	41°45′48.65″	12°40′00.62″	40.9	0.8
AH-9	S.Procula	41°40′32.43″	12°32′26.61″	41.1	1.0
$AH\text{-}3C12_{Leucite}$	1	41°45′45.40″	12°40′05.13″	41.2	1.1
$AH\text{-}3C12_{Sanidine}$	1	41°45′45.40″	12°40′05.13′	45.0	2.4
Samples included in the oldest population					
AH-3C9	1	41°45′34.07″	12°40′36.76″	68.6	1.1
AH-18C1	4	41°48′34.05″	12°34′08.09″	68.9	0.2
AH-3A	1	41°45′08.92″	12°40′58.76″	69.4	0.6

Error-weighted mean ages reported here do not include xenocrysts or data that contributed most to the mean square weighted deviation (MSWD) of the population (i.e., italicized data in Appendix A)

is quite possible that these samples contain small amounts of excess ^{40}Ar.

The oldest population of ages contains data from three different samples (see Table 1 for list). Figure 5i shows the ideogram for these data prior to dual elimination. The peak is nearly symmetrical, and the inverse isochron (Fig. 5j) produces a $^{40}Ar/^{36}Ar$ intercept (294.1±1.4) that is consistent with air. The slightly elevated MSWD of 1.7 suggests a slightly non-uniform age distribution. Dual elimination reduced the MSWD to 1.4 by eliminating one datum, and the resulting ideogram and inverse isochron are shown in Fig. 5k and l, respectively. Based on the inverse isochron results, we interpret this eruptive cycle from the Albano Maar to have an age of 69±1 ka (2σ).

Petrology

We collected indurated samples and granular mafic ejecta (see Fig. 2 for stratigraphic position) and examined them by petrographic microscope. On the basis of their freshness and stratigraphic position, we selected samples (Fig. 3) for geochemical analysis. In the following section we report petrographic observations and geochemical data (major and trace elements, $^{87}Sr/^{86}Sr$, and $\delta^{18}O$) for the selected samples. See Appendix B for details of the methods used.

Microtextural features

Modal analyses of indurated samples show that they are composed volumetrically of 50–70% matrix, 6–20% phenoclasts, 2–15% lithic clasts, and 3–20% juvenile clasts.

The matrix is zeolitised and contains microcrystalline calcite. Some samples also contain large chabazite crystals and vesicles filled with calcite and zeolite crystals (e.g. vesiculated tuff).

Phenoclasts include, in order of abundance: up to millimeter-scale clinopyroxene many containing melt inclusions, leucite some with high concentration of melt inclusions (Fig. 6a), phlogopite, magnetite, apatite, garnet, spinel, olivine, scarce sanidine, and, commonly, phenoclasts of calcite (Fig. 6b). One "vesiculated" fragment of sparry calcite (Fig. 6c) was found.

Lithic clasts are either carbonate or volcanic. Among the volcanic clasts are abundant granular vitrophyric clinopyroxenites, with rounded sparry calcite crystals in the intracumulus glass (Figs. 6d and e).

The juvenile clasts include:

1. Millimeter-scale, porphyritic, and scarcely vesiculated scoria clasts with abundant, fractured, light brown glass, leucite, scarce zoned clinopyroxene, magnetite, chabazite, and calcite crystals in the vesicles (Fig. 6f).
2. Sub-millimeter, blocky, light brown, aphyric, and vesiculated glass (Fig. 6g).
3. Centimeter-scale, porphyritic, scarcely vesiculated scoria clasts occurring at the base and in the first few meters of the Peperino Albano deposit (sites 2 and 2′ in Figs. 1, 2b, and 3). Unlike other scoria clasts from Albano, these are large enough to be studied in detail. They are porphyritic (phenocrysts 41 vol%). and characterized by cryptocrystalline zeolitised groundmass. Phenocrysts include clinopyroxene (22 vol%), leucite (12 vol%), phlogopite (4.9 vol%), garnet (0.8 vol%) and accessory minerals (1.3 vol%). Based on optical features, clinopyroxene crystals can be divided in two populations. The first population are fractured, light green, centimeter-scale, with pitted surfaces filled with glass, apatite, and phlogopite. Crystals of the second population are subcentimeter, sub-euhedral to euhedral, pleochroic (green to light brown) with glass, apatite, magnetite, and phlogopite inclusions, and frequently garnet intergrowths.

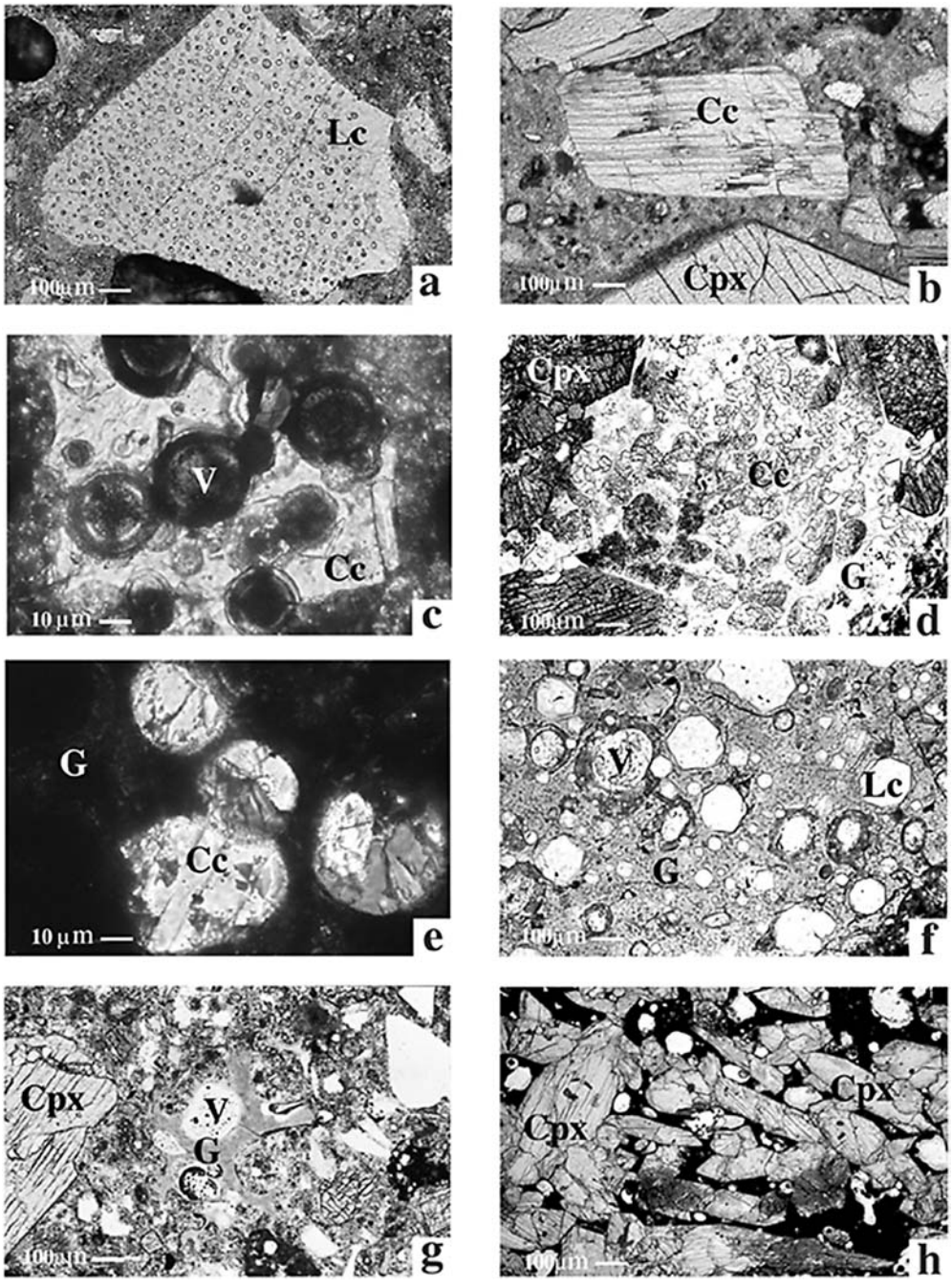

Fig. 6 Thin section photomicrographs (*Lc* = leucite; *Cc* = calcite; *Cpx* = clinopyroxene; *V* = vesicle; *G* = glass). (**a**) Melt inclusions-bearing leucite phenoclast from sample AH-3C12. (**b**) Calcite phenoclast from sample AH-3A. (**c**) Sparry calcite in sample AH-3A, vesicles filled with zeolite crystals. (**d**) Granular vitrophyric clinopyroxenite with rounded sparry calcite in the intracumulus glass, sample AH-3C12. (**e**) Detail of the rounded sparry calcite crystals, sample AH-3AX1. (**f**) Porphyritic glassy scoria clast with abundant leucite crystals, sample AH-3C8. (**g**) Aphyric vesiculated glass, sample AH-3C12. (**h**) Adcumulate clinopyroxenite, sample AH-17

Leucite crystals are centimeter sized, from anhedral to euhedral and characterized by inclusions of melt, green clinopyroxene, garnet, elongated apatite, phlogopite, and metal oxides. Phlogopite crystals are sub-centimeter sized, from sub-euhedral to euhedral, and sometimes bent. Garnet crystals are millimeter sized, from sub-euhedral to euhedral, red-brown to light brown, and have melt inclusions and pits filled of glass. Accessory minerals are millimeter-scale sub-euhedral magnetite and rare amphibole.

Modal analyses of granular mafic ejecta show two different compositions: olivine-bearing clinopyroxenite (AH-3AX1) and clinopyroxenite (AH-17, Fig. 6h). The olivine-bearing clinopyroxenite, occurring in Subunit a-2 at the base of the Albano sequence (Reference section, Figs. 2 and 3), is an orthocumulate (i.e. a cumulate rock made up of more than one mineral) containing millimeter-sized clinopyroxene (67 vol%) and olivine crystals (25 vol%), intracumulus glass (8 vol%), and rare calcite. The olivine crystals, some poikilitically enclosed in clinopyroxene, have glass-filled pits in which rounded calcite crystals are present (Fig. 6e). The clinopyroxenite is an adcumulate (i.e. a cumulate rock made up of only one mineral) with rare (<5 vol%) vesiculated and zeolitised glass occurring in the Peperino Albano (site 3 in Figs. 1 and 3).

Table 2 Electron microprobe analyses of interstitial glasses from juvenile clasts and from granular olivine-clinopyroxene cumulate (AH-3AX1), and of melt inclusions in clinopyroxenes. Compositions of glass and melt inclusion are based upon multiple analyses whose number is reported in parenthesis

Age	69±1 ka								39±1 ka										36±1 ka			
Sample	AH-3AX1		AH-3A		AH-18C1		AH-3C8		AH-3C12		AH-9				AH-3C13		AH-3C14		AH-3C16/4Fb			
Group	GI		GII		GII		GIV		GII		GII				GIV		GII		GII		GIII	
type	glass		m. inclusion		glass		glass		glass		glass	m. inclusion			glass		glass		m. inclusion		glass	
		σ (4)*		σ (9)		σ (5)		σ (13)		σ (9)			σ (10)			σ(4)		σ (3)		σ (12)		σ (3)
SiO_2	45.43	*0.38*	41.84	*1.36*	44.67	*0.26*	40.78	*0.59*	45.82	*0.36*	46.80	47.21	*1.43*		40.64	*0.59*	42.54	*0.28*	45.71	*1.10*	47.03	*1.59*
TiO_2	1.09	*0.06*	0.97	*0.12*	0.79	*0.00*	0.99	*0.14*	0.88	*0.05*	0.91	0.65	*0.07*		0.96	*0.18*	1.00	*0.08*	0.80	*0.15*	1.17	*0.15*
Al_2O_3	15.93	*0.13*	17.86	*0.63*	17.26	*0.07*	17.46	*0.88*	18.73	*0.40*	18.37	19.74	*0.46*		17.13	*0.19*	16.46	*0.18*	20.19	*0.85*	20.68	*0.54*
Cr_2O_3	0.02	*0.02*	0.04	*0.05*	0.03	*0.04*	0.04	*0.05*	0.04	*0.05*	0.20	0.02	*0.03*		0.02	*0.02*	0.02	*0.02*	0.04	*0.06*	0.00	*0.00*
FeO	8.04	*0.18*	7.58	*0.54*	7.14	*0.11*	9.10	*0.99*	7.65	*0.36*	7.34	5.81	*0.81*		9.87	*0.42*	8.59	*0.09*	6.43	*1.62*	7.00	*0.40*
MnO	0.20	*0.04*	0.21	*0.08*	0.19	*0.02*	0.24	*0.07*	0.22	*0.05*	0.09	0.20	*0.06*		0.30	*0.10*	0.19	*0.10*	0.22	*0.07*	0.47	*0.01*
MgO	5.18	*0.42*	1.63	*0.83*	2.42	*0.03*	2.58	*0.34*	1.89	*0.35*	1.91	1.23	*0.46*		1.56	*0.40*	3.10	*0.03*	1.11	*0.33*	0.48	*0.21*
CaO	12.79	*0.44*	10.12	*0.87*	9.15	*0.14*	13.39	*1.31*	9.07	*0.43*	7.88	6.47	*1.04*		11.49	*0.48*	10.83	*0.16*	7.47	*0.98*	9.16	*2.24*
Na_2O	2.29	*0.12*	2.25	*0.39*	3.13	*0.01*	4.54	*0.37*	3.08	*0.37*	2.99	2.92	*0.56*		4.77	*0.44*	2.33	*0.04*	3.56	*0.64*	6.69	*0.32*
K_2O	5.62	*0.12*	7.64	*0.74*	7.84	*0.32*	6.93	*0.97*	9.15	*0.37*	8.45	8.17	*0.70*		7.75	*0.45*	8.80	*0.08*	9.66	*1.32*	6.17	*0.91*
BaO	0.03	*0.03*	0.09	*0.06*	0.05	*0.02*	0.10	*0.04*	0.09	*0.04*	0.10	0.12	*0.02*		0.09	*0.02*	0.08	*0.01*	0.13	*0.04*	0.17	*0.00*
SrO	0.04	*0.05*	0.09	*0.04*	0.04	*0.00*	0.22	*0.09*	0.04	*0.05*	0.00	0.01	*0.03*		0.25	*0.06*	0.04	*0.05*	0.14	*0.08*	0.38	*0.12*
P_2O_5	0.42	*0.02*	0.86	*0.20*	0.58	*0.06*	0.52	*0.09*	0.38	*0.10*	0.64	0.29	*0.22*		0.66	*0.33*	0.71	*0.05*	0.31	*0.32*	0.04	*0.02*
SO_3	0.55	*0.04*	1.42	*0.13*	0.68	*0.10*	1.18	*0.44*	1.24	*0.13*	1.29	0.89	*0.12*		1.50	*0.10*	1.37	*0.07*	1.05	*0.21*	0.53	*0.10*
F	0.29	*0.10*	0.50	*0.19*	0.24	*0.03*	0.48	*0.13*	0.27	*0.12*	0.26	0.33	*0.05*		0.35	*0.05*	0.28	*0.14*	0.47	*0.23*	0.70	*0.12*
Total	97.92		93.10		94.21		98.55		98.55		97.23	94.06			97.34		96.34		97.29		100.67	

*σ is the one-sigma standard deviation; the number in parenthesis represents the number of analyses for each composition

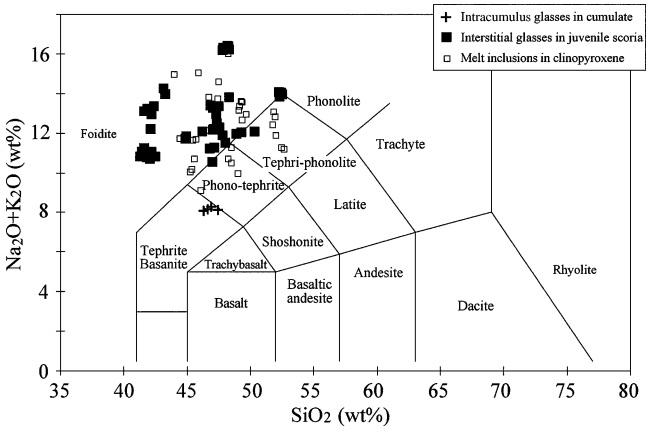

Fig. 7 Chemical composition (obtained through electron microprobe analyses, Table 2) of interstitial glasses from granular olivine-clinopyroxene cumulate and from juvenile clasts, and of melt inclusions in clinopyroxenes plotted on the Total Alkali Silica diagram

Phase Composition

Glass

In Table 2 we report the chemical composition of glasses occurring in juvenile clasts and olivine-bearing clinopyroxenite and that of melt inclusions occurring in clinopyroxenes. Glasses in juvenile clasts and melt inclusions have MgO<3 wt%, Al_2O_3>17 wt%, and CaO>8 wt% and can be considered evolved ultrapotassic magmas (Foley et al. 1987). Intracumulus glass from olivine-bearing clinopyroxenite is characterized by the highest MgO content (5.18 wt%) and can be classified as primitive ultrapotassic melt (Foley et al. 1987). In particular, interstitial glasses from juvenile clasts plot in the foiditic field of the total alkali-silica diagram, melt inclusions plot across foiditic, phono-tephritic, and tephri-phonolitic fields, while intracumulus glass from olivine-bearing clinopyroxenite plot in the tephrite field (Fig. 7). Albano samples also follow the differentiation trend typical of the Alban Hills rock types (Trigila et al. 1995). This peculiar trend, characterized by a constant/decreasing amount of silica, cannot be discerned by using the SiO_2 content as a differentiation index (e.g. Total Alkali Silica diagram, Fig. 7). In contrast, when using the Na_2O (cf. Palladino et al. 2001) and MgO contents, glasses of the Albano samples can be divided in four different groups (Fig. 8a). It is important to stress that the four groups are defined on the basis of their degree of petrological differentiation, not following their ages. However, it is worth nothing that the most primitive glass belongs to the oldest sample and the most differentiate glass belongs to the youngest.

The most primitive group (GI) is represented by the intracumulus glass from olivine-bearing clinopyroxenite. This glass shows low Na_2O and K_2O and the highest MgO contents (Fig. 8a) and is comparable to the bulk composition of the most primitive Alban Hills lava flows (Peccerillo et al. 1984; Trigila et al. 1995). It is worth noting that this group, although primitive, does not show the lowest amount of silica (Fig. 8b).

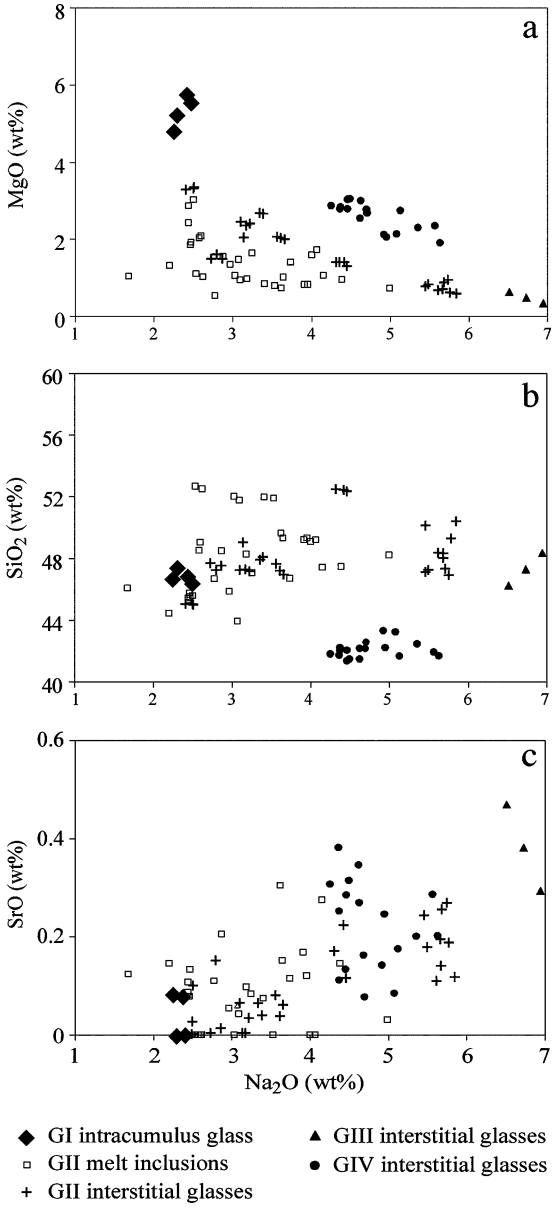

Fig. 8 Variation diagrams of MgO (**a**), SiO_2 (**b**), and SrO (**c**) vs. Na_2O (on a water-free basis) of glasses from juvenile clasts and from olivine-clinopyroxene cumulate, and of melt inclusions in clinopyroxenes. Because of their peculiar composition (e.g., low silica content and lack of modal plagioclase) the best differentiation index to define the Alban Hills primitive and differentiated rocks is the Na_2O content (Palladino et al., 2001). All data were obtained through electron microprobe analyses (Table 2). Group I includes sample AH-3AX1; Group II includes samples AH-3A, AH-18C1, AH-9, AH-3C12, and AH-3C14; Group III includes sample AH-3C16/4Fb; Group IV includes samples AH-3C8 and AH-3C13. Groups are defined on the basis of their chemical composition, not on the basis of their ages

The second group (GII) includes aphyric blocky glass and melt inclusion from clinopyroxenes and is characterized by a wide range of Na_2O, constant SiO_2 (Fig. 8b), and high K_2O contents. Chemical compositions of these glasses are comparable to that of the fiamme of the last large pyroclastic eruption of the Tuscolano-Artemisio Phase (Upper Flow Unit of Villa Senni Eruption, Freda et al. 1997).

Table 3 Representative electron microprobe analyses of major elements in clinopyroxenes

Age	69±1 ka					39±1 ka		36±1 ka		
Sample	AH-3AX1	AH-3A		AH-3C8		AH-9		AH- 3C16/4Fb		AH-17
Group	GI	GII		GIV		GII		GIII		adcumulate
	core	core3	core1	core	rim	core3	core2	core1	core4	core
Ox wt%										
SiO_2	52.72	52.80	45.88	53.04	44.02	52.37	52.17	49.66	37.92	48.12
TiO_2	0.38	0.28	1.27	0.37	1.30	0.32	0.42	0.82	2.68	0.96
Al_2O_3	2.73	2.17	7.24	2.18	8.85	1.91	2.48	4.66	12.42	5.58
Cr_2O_3	0.49	0.70	0.01	0.49	0.00	0.17	0.14	0.00	0.04	0.10
FeO	3.10	2.75	7.14	3.22	9.03	3.29	3.98	5.67	15.49	6.82
MnO	0.13	0.06	0.07	0.11	0.06	0.06	0.11	0.13	0.25	0.08
MgO	15.97	17.27	12.64	16.60	10.94	17.11	16.27	14.34	6.29	13.53
CaO	24.92	23.79	24.12	24.76	24.65	24.04	24.08	24.78	23.63	24.38
Na_2O	0.05	0.15	0.19	0.13	0.23	0.16	0.14	0.13	0.32	0.18
K_2O	0.00	0.01	0.01	0.00	0.03	0.00	0.00	0.05	0.00	0.02
Total	100.49	99.98	98.57	100.90	99.11	99.43	99.79	100.24	99.04	99.77
atomic formula unit										
Si	1.918	1.920	1.724	1.918	1.657	1.915	1.910	1.825	1.471	1.783
Ti	0.010	0.008	0.036	0.010	0.037	0.009	0.012	0.023	0.078	0.027
Al^{IV}	0.082	0.080	0.276	0.082	0.343	0.085	0.090	0.175	0.529	0.217
Al^{VI}	0.036	0.013	0.045	0.011	0.050	0.000	0.017	0.027	0.039	0.027
Cr	0.014	0.020	0.000	0.014	0.000	0.005	0.004	0.000	0.001	0.003
Fe^{3+}	0.015	0.043	0.174	0.046	0.237	0.076	0.056	0.115	0.356	0.147
Fe^{2+}	0.080	0.040	0.050	0.051	0.047	0.024	0.066	0.059	0.146	0.064
Mn	0.004	0.002	0.002	0.003	0.002	0.002	0.003	0.004	0.008	0.002
Mg	0.866	0.936	0.708	0.895	0.614	0.933	0.888	0.786	0.364	0.748
Ca	0.972	0.927	0.971	0.960	0.994	0.942	0.945	0.976	0.982	0.968
Na	0.004	0.011	0.014	0.009	0.017	0.011	0.010	0.009	0.024	0.013
K	0.000	0.000	0.000	0.000	0.001	0.000	0.000	0.002	0.000	0.001
Total	4.000	4.000	4.000	4.000	4.000	4.000	4.000	4.000	4.000	4.000
Mg^*	0.796	0.835	0.549	0.817	0.462	0.827	0.787	0.663	0.241	0.608

Mg^*: $Mg/(Mg+Fe_{tot}+Al_{tot}+Ti)$

The third group (GIII) is represented by interstitial glasses from the Peperino Albano scoria clasts and is characterized by the highest Na_2O and lowest MgO contents (Fig. 8a); its chemical composition is different from any other Alban Hills product. However, these glasses are in equilibrium with Ti-andradite crystals that typically occur in the granular hypoabyssal rocks ("italites", Gaeta et al. 2000) interpreted as representative of magma crystallizing in contact with an endoskarn (Einaudi et al. 1981). The GIII glasses represent the most differentiated Albano products as confirmed also by their highest SrO content (Fig. 8c). Indeed, in the Alban Hills volcanic products, because of the lack of plagioclase crystallization, Sr behaves as an incompatible element and can be used to document the evolution of magmas. In contrast, melt inclusions occurring in clinopyroxenes from the Peperino Albano scoria clasts show a more primitive composition characterized by lower Na_2O and SrO, and it falls in the GII field (Fig. 8a, b, c).

The fourth group (GIV) is interstitial glass from porphyritic juvenile clasts enriched in leucite microcrysts (Fig. 6f) and is characterized by intermediate Na_2O and the lowest SiO_2 content (Fig. 8b); this glass has a chemical composition comparable to the oldest and largest Alban Hills lava flow (Vallerano lava flow, Trigila et al. 1995).

Clinopyroxene

We report data for clinopyroxenes (Tables 3, 4, and 5) sampled in the juvenile scoria clasts and in the mafic cumulates. Since the clinopyroxenes from the Alban Hills products have very high and constant CaO ($0.95<Ca>1$ atomic formula unit, hereafter afu) and high Al_2O_3 contents, the Wo-En-Fs and Q-J ($Q=Ca+Mg+Fe^{2+}$; $J=2Na$) diagrams (Morimoto et al. 1988) are not ideal to show their chemical variation. We found the Si vs. $Mg/(Mg+Fe_{tot}+Al_{tot}+Ti)$ (hereafter Mg^*) diagram more suitable to present the enrichment in Ca-Tschermak's and CaFe-Tschermak's components of Albano clinopyroxenes. In this diagram clinopyroxenes show a wide compositional range due to coexistence within the same sub-unit of zoned crystals and different populations.

Clinopyroxenes from samples AH-3AX1, AH-3A (Subunit a-1, Fig. 2) and AH-9 (Santa Procula, Fig. 1) show high Si and Mg^* values (Fig. 9) with just one exception

Table 4 Representative analyses (Laser Ablation-ICP-MS) of trace elements in clinopyroxenes. See Appendix B for analytical details

Age	69±1 ka		39±1 ka		36±1 ka
Sample	AH-3A		AH-9		AH-17
Group	GII		GII		adcumulate
	core3	core1	core3	core2	core1
ppm					
Sc	86	106.68	85.99	92.69	79.81
V	91.2	207.23	90.21	122.48	169.66
Cr	5114.02	35.75	2963.06	431.97	217.8
Co	23.17	33.02	25.89	32.99	41.04
Sr	145.25	272.45	195.92	191.18	185.63
Y	4.69	18.03	5.69	7.94	9.1
Zr	11.6	320.58	27.83	41.96	76.35
Nb	0.0206	0.552	0.0466	0.0972	0.1064
La	2.98	13.33	4.4	5.63	7.62
Ce	10.73	49.9	16.37	18.93	33.1
Pr	1.83	8.4	2.87	3.3	5.28
Nd	10.2	43.14	14.2	16.98	26.75
Sm	2.53	10.09	3.72	3.99	5.88
Eu	0.615	2.096	0.698	0.845	1.27
Gd	2.03	7.45	3.04	3.08	3.49
Tb	0.226	0.843	0.299	0.364	0.479
Dy	1.346	3.92	1.591	1.893	2.32
Ho	0.207	0.617	0.275	0.32	0.325
Er	0.464	1.514	0.378	0.676	0.94
Tm	0.0683	0.1954	0.0641	0.0903	0.107
Yb	0.364	1.085	0.461	0.567	0.71
Lu	0.0511	0.1596	0.0621	0.0883	0.102
Hf	0.612	13.38	1.627	1.957	4.15
Ta	0.0111	0.0814	0.0084	0.0076	0.0349
Pb	0.253	0.242	0.276	0.167	0.285
Th	0.069	0.617	0.1055	0.1431	0.265

Table 5 Representative analyses of $^{87}Sr/^{86}Sr$ and $\delta^{18}O$ in clinopyroxenes. See Appendix B for analytical details

Age	Sample	Group	$^{87}Sr/^{86}Sr$	2σ	$\delta^{18}O$	$1\sigma(n)$
69±1 ka	AH-3A, 3*	GII			6.02	*0.02 (3)*
	AH-3A, 1*	GII			6.93	*0.21 (3)*
	AH-3A, 5	GII	0.708508	*0.000010*		
	AH-3A, 4	GII	0.709416	*0.000009*		
39±1 ka	AH-9, 3*	GII			6.57	*0.04 (2)*
	AH-9, 2*	GII			6.08	*0.14 (4)*
	AH-9, 5	GII	0.709621	*0.000009*		
	AH-9, 4	GII	0.709675	*0.000009*		
36±1 ka	AH-3C16/4Fb	GII	0.709579	*0.000010*	6.37	*0.01(2)*
	AH-17, 1*	adcumulate	0.709544	*0.000010*	5.53	*0.21 (2)*

*same crystals as in Table 3

showing lower Si content. These clinopyroxenes also show the highest Cr_2O_3 content (0.70 wt%) analysed in clinopyroxenes from the Alban Hills deposits (Trigila et al. 1995) to date. The clinopyroxenes occurring in olivine-bearing clinopyroxenite are associated with GI type glass (Table 3, Fig. 9), while melt inclusions occurring in clinopyroxenes from AH-3A and AH-9 belong to the GII composition. In the scoria clast AH-3C16/4Fb (Subunit f-1, Fig. 2) two populations of clinopyroxene are present. The first population, represented by very few crystals, is not in equilibrium with the melt (see microtextural section) and shows intermediate Si and Mg* values. Clinopyroxenes of the second population are well represented in both the juvenile scoria clasts and the matrix. These clinopyroxenes, enriched in Fe, Al and Ti (low Mg*) and depleted in Si, are associated with GIII type glasses. Clinopyroxenes occurring in sample AH-3C8 (Subunit b-2, Fig. 2) are associated with GIV glasses and show a strong compositional zoning with the cores having high Si and Mg* values while the rims, usually very thin, have lower Si content and are enriched in Fe, Al,

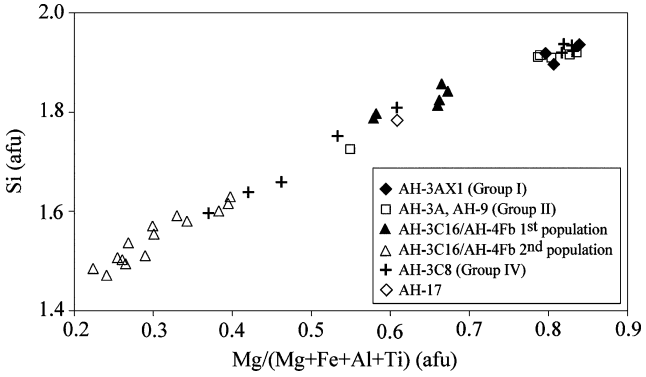

Fig. 9 Si vs. Mg/(Mg+Fe_{tot}+Al_{tot}+Ti) (expressed in atomic formula unit) diagram for clinopyroxenes sampled in the juvenile scoria clasts and in the mafic cumulates (AH-3AX1 and AH-17). All data were obtained through electron microprobe analyses (Table 3)

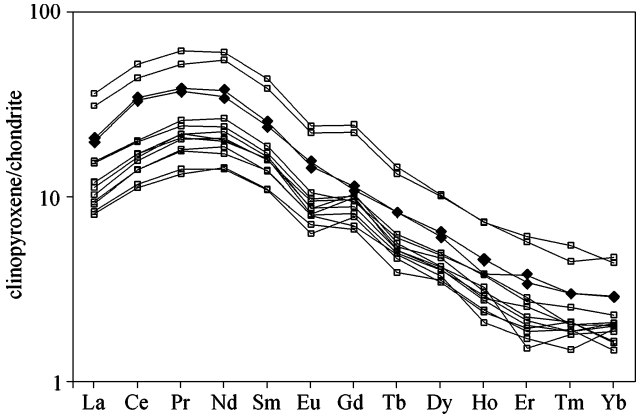

Fig. 10 Rare Earth Elements in clinopyroxenes showing a convex upward parallel trend (analytical methods in Appendix B). REE normalised to chondrite C1 sample (Sun and McDonough 1989). Data in Table 4. Empty squares refer to juvenile pyroclastic clinopyroxenes (AH-3A and AH-9 samples); filled diamonds refer to clinopyroxenes from adcumulate sample (AH-17)

and Ti. Clinopyroxenes occurring in adcumulate (AH-17) are characterized by intermediate Si and Mg* values.

Clinopyroxenes are the sole ubiquitous mineralogical phase able to record the variation of the Alban Hills magmas during petrological evolution. Thus, in order to obtain additional petrological constraints, we performed single crystal trace element (Table 4) and isotopic (Table 5) analyses on selected clinopyroxenes from Albano. Some Mg*- and Si-rich clinopyroxenes have a Cr content compatible to that measured in the bulk composition of the Alban Hills primitive lava flows (Peccerillo et al. 1984). The Cr content is directly correlated with the Si and Mg* decrease. In contrast, due to their incompatible behavior in the Alban Hills magmas, Th, Zr, Y, Sr, and REE increase when Si and Mg* values decrease. These trends confirm that Si and Mg* values give constraints on magma differentiation. Moreover, the Albano clinopyroxenes show parallel convex-upward chondrite-normalized REE patterns (Fig. 10), characterized by a high and constant LREE/HREE ratio (La/Yb=9.25; σ=1.56). The $^{87}Sr/^{86}Sr$ ratio of the Albano clinopyroxenes (Table 5) is lower than the typical value (0.710) of older (>70 ka) Alban Hills lavas and scoria (Ferrara et al. 1985) and is in agreement with the $^{87}Sr/^{86}Sr$ ratio measured in the bulk composition of sialic granular xenoliths occurring in the same deposits (Federico et al. 1994). Albano clinopyroxenes show $\delta^{18}O$ values ranging from 5.53 to 6.93‰ (Table 5). Clinopyroxenes showing the highest $\delta^{18}O$ value are also characterized by the highest REE contents (Tables 4 and 5).

Other phases (selected microprobe analyses are available on-line as supplementary data). Leucite, together with clinopyroxene, is the most abundant mineralogical phase in the Alban Hills products. Leucite is quasi-stoichiometric with low Na_2O (<0.58 wt%) and BaO contents (<0.20 wt%) and FeO content up to 0.50 wt%. Olivines (CaO=0.4–0.7 wt%) occur in the orthocumulates (Fo_{87}) and in the matrix (Fo_{90}) of the Subunit a-3 (Reference section, Fig. 2) and have $\delta^{18}O$ values ranging from 6.98 to 7.16‰ (Dallai et al. 2004). Phlogopite, characterized by relatively high BaO (up to 0.60 wt%) and F (up to 0.80 wt%) contents, is comparable to that occurring in the pre-Albano scoria clasts (Gaeta et al. 2000). Amphiboles are rare in the Alban Hills products. This mineral was found only in a few lava flows (Gaeta and Freda 2001) and granular ejecta (Federico et al. 1994). The amphibole occurring in the Albano scoria clasts is a Mg-hastingsite with relatively high K_2O (up to 3 wt%) and F (up to 0.8 wt%) contents. The SrO and F contents are lower compared to amphiboles occurring in the lava groundmass. Phlogopite and amphibole show a similar F/OH (up to 0.25) ratio, indicating a water activity in the magma lower than 1; this feature is also confirmed by the apatite composition (high F and SO_3 contents). Garnet, usually rare in the Alban Hills scoria clasts, is abundant in all the Albano products and particularly in the scoria clasts. It can be classified as Ti-andradite (TiO_2 up to 7 wt%) and it is characterized by a weak Si and Al increase and Ti and Fe decrease from core to rim. These chemical features and its intergrowth with Si-poor clinopyroxene and glass, clearly indicate a magmatic origin. Magnetite has an ulvospinel content of 14–15 mol%. The coexistence of garnet and clinopyroxene, as well as the ulvospinel content in magnetite, indicate an oxygen fugacity between the NNO and MH buffers (Gustafson, 1974; Spencer and Lindsley, 1981) in the differentiated Albano magmas.

Discussion

Eruptive history

Stratigraphic breaks within the Albano succession witness several distinct episodes of volcanism from the multiple maar. As shown in the Geochronology section, $^{40}Ar/^{39}Ar$ ages reveal three age groups at 69±1, 39±1, and 36±1 ka (Fig. 11). These data suggest that the several episodes of volcanism were not evenly distributed in time, but occurred during two major eruptive cycles, with the second cycle including two sub-cycles. The youngest

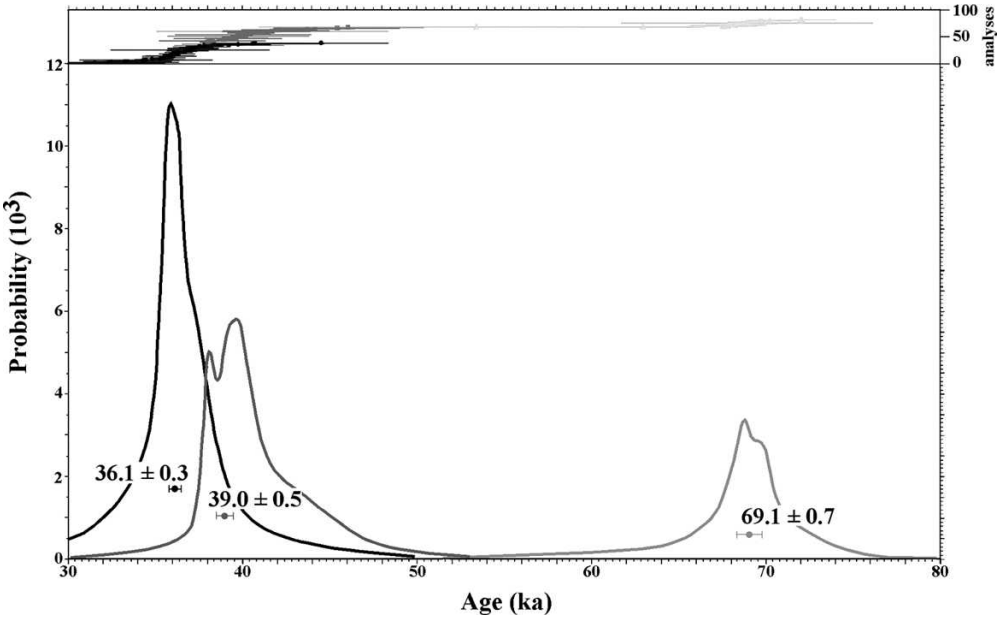

Fig. 11 Summary ideogram of the three eruptive cycles from the Albano Maar, using 2σ error distributions

eruption age corresponds to the samples of Peperino Albano. We consider the geochronology-based distinction in eruptive cycles to be the first-order evolutionary history of Albano Maar. Each cycle is bracketed by two significant stratigraphic breaks in the field (Figs. 2 and 3). Within these major eruptive cycles, the other intervening lithostratigraphic evidences of breaks mark second-order events (i.e. individual eruptions and eruptive episodes) not resolved with our $^{40}Ar/^{39}Ar$ age data.

The bathymetry of Albano Lake (Caputo et al. 1986) indicates three overlapping main craters (Fig. 12); the smallest and youngest of these craters, in the SE part of the lake, excavated the center of a previous one that, in turn, dissected the rim of the oldest one. We tentatively relate the two larger craters and their evolution with the occurrence of two major eruptive cycles. The smallest, youngest crater is attributable to the last eruptive event of the second cycle.

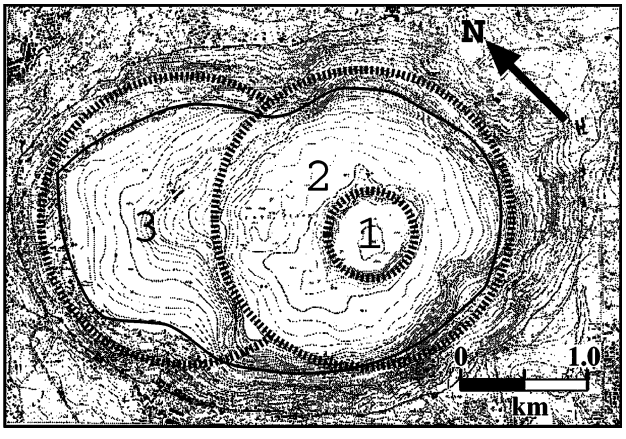

Fig. 12 The bathymetry of the Albano Lake indicates three main craters: the smallest and youngest (1) located in the centre of an older one (2) that, in turn, cut the rim of the oldest one (3). Modified after Caputo et al. (1986)

The first cycle (69±1 ka) produced the lower 66-m-thick suite of deposits of the Reference section. Only one incipiently pedogenised ash layer divides the succession at 27 m, suggesting the presence of at least two separate eruptions (Units a and b). In these eruptions, prolonged magma-water interaction deposited a thick surge succession and excavated a new crater, as testified by the abundance of lithic breccia. The general upward transition from wet to dry products and increasing abundance of scoria fall layers (Fig. 2) is interpreted to be the result of a general decrease in the amount of interacting water during the evolution of this cycle. Partially reworked, distal products of the first cycle include the lowermost unit of the GRA/Appia Antica section (Unit GRAa). These correlate well with those of the Reference section by age, lithic components, and textural and petrological features. The lack of xenocrysts in these samples suggests that local reworking did not involve older products.

The activity of the second cycle (since 39±1 ka) clearly differs from that of the first one (69±1 ka). Two incipiently pedogenised ash layers and geochronological-petrological data indicate the occurrence of at least four different eruptions (Units c, d, e, and f in Fig. 2), and new crater excavation enriched the deposits in lithic clasts. Eruptions of the second cycle appear to be more energetic than those of the first one. At the same distance from the vent, the deposits are coarser-grained, and meter-scale dune-like structures and dm-scale layering replaces ripples and cm-scale laminations. Also, the occurrence in the distal outcrops of products from the different units suggests that those from the second cycle, and particularly those from the 39±1 ka eruption, had a widespread distribution. At the GRA/Appia Antica section the massive deposit in the middle of the section (Unit GRAb), correlates with these products. The lack of xenocrysts suggests only syn-eruptive reworking for this unit. The same conclusion is inferred for the lower, massive unit recognized in the

bore cores of Casale Ferranti. In contrast, the uppermost unit at this site contains crystals yielding ages of the older Villa Senni Eruptive Sequence and of the Monte delle Faete Phase of activity; only two ages, which when combined produce an error-weighted mean age of 38.2±0.3 ka, are likely to represent juvenile crystals. These ages, and the absence in this deposit of crystals yielding ages of the Peperino Albano eruption, suggests that it may correlate with the similar 39±1 ka reworked products of Unit GRAb. Finally, also the deposit of Santa Procula (41±1 ka, Marra et al. 2003) can be attributed to variably reworked products of the 39±1 ka eruption of the second cycle.

The most recent sub-cycle recognized so far occurred at 36±1 ka and perhaps includes only one eruption. Its deposits, including Peperino Albano, are in places similar to those of the previous eruptive events of the second cycle, but, notably, they are the only ones that contain up to dm-sized, vesicular scoria clasts. The scoria clasts, however, are not present in the distal, reworked equivalent at the GRA/Appia Antica section, nor are they in the type-locality for the Peperino Albano (Valle delle Petrare outcrops). Here, sample AH-17C3 yielded the age of 36.1±0.3 ka, in agreement with a previous sample from a building stone of the Carcere Mamertino in Rome (sample MAM-01, 36.0±1.2 ka, Karner et al. 2001a). One sample from the upper horizon (Unit GRAc) at the GRA/Appia Antica section also yielded the same age. Based on the presence of rounded clasts and a few contaminant crystals in Unit GRAc, we interpret it to be a reworked equivalent to the Peperino Albano. Note that xenocrysts occur mainly in the samples of Peperino Albano collected from the distal locations, which are expected for pyroclastic deposits that flow long distances over the landscape.

The GRA/Appia Antica section is also described in Funiciello et al. (2003) and Soligo et al. (2003), while Funiciello et al. (2002) describe at a different locality (Lucrezia Romana) the same products that we have recovered from bore cores in the adjacent Casale Ferranti site. These authors propose different geochronologic and stratigraphic correlations based on a U-Th age of 23±6.7 ka on a carbonate layer underlying the volcaniclastic succession and a ^{14}C age of ~5100 yrs BP on a soil underlying the uppermost unit. Other authors report younger eruptions from Albano (Fornaseri and Cortesi 1989; Villa et al. 1999) than those reported here. These ages conflict with our geochronological and petrographic evidence. We believe that our age data, directly recording magma crystallization, are the most suitable for describing the eruptive history of the center. Moreover, we specifically sampled the topmost stratigraphic products around the north-western Alban Hills, and we did not find any product younger than 36±1 ka and any crystal younger than 31.5±3.9 ka (see Appendix A). These results suggest that no younger magmatic or phreatomagmatic eruption has occurred from the Albano Maar. However, given the great relevance of this point for hazard assessment of the area, a more specific search for the youngest eruptive products of Albano is currently in progress.

Primitive magma and liquid line of descent of Albano

The petrological data obtained from this study demonstrate that the pre-eruptive system of the Albano Maar was fed by a primitive magma (i), which is different from pre-Albano magmas (ii) and originated from an enriched mantle source (iii).

i) Primitive olivine ($Fo_{85–90}$) and diopside (Cr-bearing) occur at the beginning of the eruptive sequence (Subunit a-1 and a-2). According to the solid-liquid partition coefficients for trace elements (Hart and Dunn 1993), these phases were in equilibrium with a primitive melt comparable to the less differentiated Alban Hills lava flows (Peccerillo et al. 1984; Trigila et al. 1995).

ii) The LREE/HREE and $^{87}Sr/^{86}Sr$ ratios of primitive clinopyroxenes from Albano products do not overlap those of pre-Albano eruptions (Fig. 13), suggesting chemical variation of the Albano primitive magma. In particular, the $^{87}Sr/^{86}Sr$ ratio of Albano magma indicates a chemical variation in the magma source. Pre-Albano volcanic products (lava flows, scoria clasts, and clinopyroxenes), indeed, are characterized by $^{87}Sr/^{86}Sr$ always higher than 0.710 (Ferrara et al. 1985; Gaeta et al. 2005), while $^{87}Sr/^{86}Sr$ ratio of clinopyroxenes from the Albano deposits are significantly lower (Table 5). Notably, the relatively low $\delta^{18}O$ values (Table 5) of Albano primitive clinopyroxenes exclude the possibility that the $^{87}Sr/^{86}Sr$ ratio decrease was due to significant assimilation of limestone wall rocks. The amount of limestone rocks required to decrease the $^{87}Sr/^{86}Sr$ ratio from 0.710 (pre-Albano) to 0.709 (Albano), indeed, is not compatible with the measured $\delta^{18}O$ values (Table 5) and with thermodynamic calculations (Bohrson and Spera 2001).

iii) The primitive ultrapotassic magmas from the Roman Province, characterized by high $^{87}Sr/^{86}Sr$ and LREE/HREE ratios, are generally interpreted as having originated from an enriched mantle source (Peccerillo 1985; Conticelli and Peccerillo 1992; Di Battistini et al. 1998; Conticelli et al. 2002; Dallai et al. 2004; Perini et al. 2004). The high LREE/HREE ratio of the Albano clinopyroxenes (Fig. 10) suggests also for Albano primitive magmas an origin from a metasomatized peridotite. An enriched mantle source is supported also by the high $^{87}Sr/^{86}Sr$ ratio of clinopyroxenes (Table 5) and by the bulk compositions of Albano granular sialic ejecta (Federico et al. 1994).

A serious problem for petrologists studying the Alban Hills deposits is the lack of glass in juvenile products, with the only exception being fiamme occurring in the Lower Flow Unit of the Villa Senni Eruption (366±4 ka; Freda et al. 1997). The lava flow groundmass, indeed, is holocrystalline and the scoria clasts groundmass is cryptocrystalline and zeolitised. In contrast, Albano pyroclastic deposits

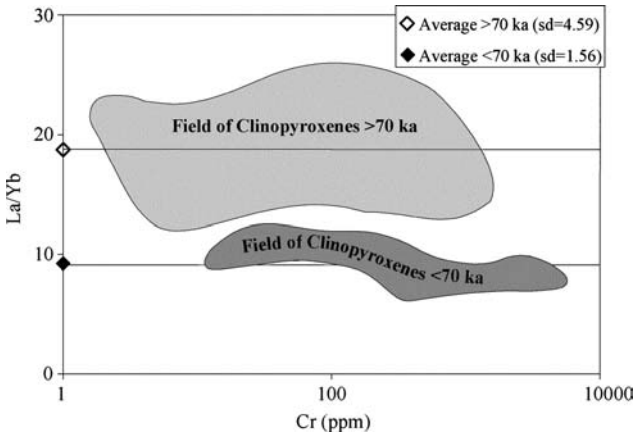

Fig. 13 La/Yb vs. Cr diagram of clinopyroxenes from Albano activity (*dark grey field*) and of pre-Albano activity (*grey field*; data from Dallai et al. 2004). Analytical methods in Appendix B. *Lines, with open diamond and filled diamond symbols*, represent the average value of La/Yb ratio in pre-Albano and Albano clinopyroxenes, respectively. Clinopyroxenes older and younger than 70 ka show a $^{87}Sr/^{86}Sr$ ratio higher and lower than 0.710, respectively (Gaeta et al. 2005)

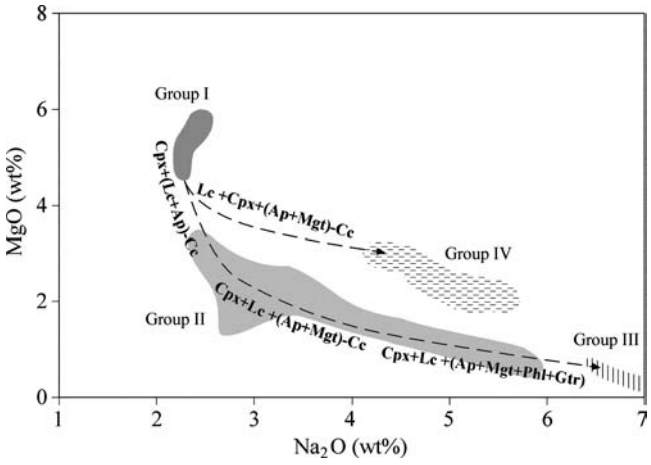

Fig. 14 Sketch of the Albano liquid line of descent. The various grey fields were drawn excluding the analyses of melt inclusions, see text for details and Fig. 8 for the list of samples included in each Group. In brackets, we report the accessory mineralogical phases

commonly have fresh juvenile vitrophyric products and also glass-bearing cumulate that are common in other volcanic districts (Hermes and Cornell 1981). Therefore, our petrologic study of Albano glasses defines the liquid line of descent of the Albano pre-eruptive magmatic system. According to the constant LREE/HREE (Fig. 13) and $^{87}Sr/^{86}Sr$ (Table 5) in clinopyroxenes, the liquid line of descent of Albano is mostly driven by a crystal fractionation process, starting from parent magmas having similar geochemical features.

We assume that the Albano liquid line of descent starts from the GI glasses (Fig. 14). These glasses occur in cumulates together with olivine and clinopyroxene and their composition is comparable to that of the most primitive Alban Hills lava flows (Peccerillo et al. 1984). However, cumulates are highly crystallized and GI glasses show a Mg# (57) lower than that typical of primitive Italian ultrapotassic rocks (Conticelli et al. 2002). In addition, the high $\delta^{18}O$ values of olivine (see "Other phases" section) and their generally scarce occurrence in cumulates and primitive lava flows indicate that, in these compositions, olivine is not a stable phase and is not involved in the differentiation of the GI glasses. In contrast with the other volcanic district of the Roman Province, the Albano differentiation process moves from parental magmas (e.g. GI) towards more evolved ones (e.g. GII; Fig. 13) without increasing the silica content (Figs. 7 and 8b) due to the absence of olivine, plagioclase (Palladino et al. 2001), and phlogopite crystallization. In Albano magmas (similarly to pre-Albano magmas), the stability field of phlogopite is reduced with respect to clinopyroxene because of the high CO_2 activity in the pre-eruptive environment. This is in agreement with the presence of well-defined CO_2 peaks (detected by Fourier Transform Infrared spectroscopy) in the GII glasses. According to the proposed model, the first step (Fig. 14) of the differentiation from GI towards GII composition is mostly driven by clinopyroxene fractionation as demonstrated also by the occurrence of clinopyroxene adcumulates (Fig. 6h) and by GII glass composition, which is comparable to that of melt inclusions occurring in clinopyroxenes. Then, other phases, such as leucite and apatite can be involved in the process (Fig. 14). However, according to mass balance calculation, the differentiation from GI towards GII is possible only if a small amount of calcite (<5 wt%) is assimilated during the clinopyroxene (±leucite and apatite) fractionation process. Due to the presence of abundant carbonate rock in the substrate, this Assimilation Fractional Crystallization process (De Paolo 1981) is realistic and, considering the small amount of calcite required, also thermodynamically possible under hypabyssal conditions (Bohrson and Spera 2001). On the other hand, calcite is a relatively common phase in the Alban Hills juvenile products, such as lavas and cumulates (see spherical calcite in Fig. 6d and e). This phase generally shows $\delta^{13}C$ and $\delta^{18}O$ values (Fornaseri and Turi 1969; Turi 1970) typical of limestone and/or thermometamorphic limestone.

According to our proposed liquid line of descent, the GII melt evolution continues by crystallization of clinopyroxene + leucite ± apatite ± magnetite coupled with the assimilation of small amounts of calcite and/or interaction with crustal CO_2 (Freda et al. 1997; Dallai et al. 2004). This kind of liquid line of descent was defined also for the pre-eruptive systems of the large explosive eruptions of the pre-Albano period (Freda et al. 1997; Palladino et al. 2001).

Finally, GII melts produce GIII melts by crystallization of clinopyroxene + leucite ± magnetite ± apatite ± phlogopite ± garnet as confirmed by mass balance calculations. Notably, as recorded also by the extreme evolved chemical compositions of clinopyroxenes (Fig. 9), the glasses (GIII) in the Peperino Albano scoria clasts are the most differentiated compositions analyzed in the Alban Hills District to date.

GIV melts do not fit the proposed liquid line of descent. We suggest that this group of melts formed during the evolution from GI to GII melts if a change in the fractionated solid occurs (i.e. decrease of the clinopyroxene/leucite ratio). This change can be related to an enlargement of the leucite stability field, as suggested by the presence of a large amount of leucite microcrysts in GIV glasses (Fig. 6f). In turn this enlargement of the leucite field can be due to a pressure drop and/or by a decrease of the H_2O activity in the melt (Gittings 1979). According to data discussed above and to Dallai et al. (2004) we suggest that the decrease of H_2O activity in Albano magmas might be induced by an increase of the CO_2 activity. A change in the conditions controlling the fractionation process is also recorded by the very thin rim with a strong compositional variation of the clinopyroxenes occurring in the group IV (Fig. 9).

It is worth noting that the matrix of some Albano indurated deposits are characterized by higher K-feldspar contents, compared to pre-Albano products (Fornaseri et al. 1963; Trigila et al. 1995; Gaeta 1998). However, microtextural and microchemical features (resorbed rims and very high BaO content, respectively) of K-feldspars occurring in the Albano samples and in granular ejecta (Federico and Peccerillo 2002) indicate that its crystallization can occur only under particular conditions. K-feldspar crystallization, indeed, is usually favored by high water activity and high BaO and SrO activity. These conditions occurred only occasionally in the Albano magmatic system and, as demonstrated by resorbed rims of K-feldspar, did not persist long enough to stabilize K-feldspar as phenocrysts in juvenile products.

Trying to correlate the petrologically-defined groups with the geochronologically-defined eruptive cycles the following appears: in the deposit of the oldest cycle (69 ka) we found GI, GII, and GIV compositions; in the intermediate subcycle (39 ka) GII and GIV; and in the youngest subcycle (36 ka) GIII only. This observation has two possible explanations: either each of the Albano main eruptive cycles started with the arrival of a new batch of magma that evolved following the above described liquid line of descent, or only one filling event and a continuous petrologic evolution process occurred during the whole life of the Albano Maar. The present data does not allow us to univocally discern between the two scenarios. We only note that the least (GI) and most (GIII) evolved compositions occur only in the oldest and youngest deposits, respectively, and that some of the processes (calcite assimilation, enlargement of the leucite stability field) surely occurred during both cycles.

Conclusions

The Albano Maar had an unforeseeably complex chronological and geochemical evolution. The activity started after the longest dormancy period in the history of the Alban Hills Volcanic District (~80 kyr, against an average recurrence period of ~45 kyr, Marra et al. 2004), and comprised two eruptive cycles separated by ~30 kyr of dormancy. Geochronological and geochemical data presented in this paper suggest that the activity of the Albano Maar represents a new magma recharge phase of the Alban Hills Volcanic District.

In particular, geochronological and geochemical data give the following insights:

i) Eruption ages of the Albano Maar products cluster at 69±1, 39±1, and 36±1 ka, defining two major eruptive cycles, the second one divided in two sub-cycles;
ii) Lack of juvenile crystals younger than 36±1 ka suggests that no magmatic or phreatomagmatic activity occurred in the Albano Maar after that time;
iii) The LREE/HREE and $^{87}Sr/^{86}Sr$ data suggest that the activity of the Albano Maar was fed by a new batch of primary magma that originated from a metasomatized mantle;
iv) The reconstructed liquid line of descent indicates that, as observed for older pre-eruptive systems of the Alban Hills, also at Albano, magma differentiation is strongly controlled by the magma/limestone wall rock interaction (see also Dallai et al. 2004).

Considering that the time elapsed since the start of the last eruptive cycle is on the same order of the average recurrence time and that the last eruption occurred 36±1 ka, we define the Alban Hills as a dormant volcanic district.

Acknowledgements Many thanks to E. Boschi and M. Cocco for supporting this research. We are grateful to M. Albano for drawing most of the figures to R. Brooker for measuring the CO_2 content in some samples through Fourier-Transform Infrared technique, and to M. Serracino for technical assistance during microprobe analyses. The final version of the manuscript was improved thanks to J. Donnelly-Nolan, M. Ort, M. Lanphere, and K. Bell revisions. Porchetta de Ariccia provided fundamental support to field work

Appendix A

$^{40}Ar/^{39}Ar$ age data

Lab. No	Sample ID	# of crystals	$^{36}Ar/^{39}Ar$	$^{37}Ar/^{39}Ar$	$^{38}Ar/^{39}Ar$	$^{40}Ar/^{39}Ar$	^{40}Ar moles x10^{-15}	$\%^{40}Ar^{*a}$	$^{40}Ar^{*a}/^{39}Ar$	s $^{40}Ar^{*a}/^{39}Ar$	Age (Ma)	$\pm1\sigma^{d}$	Irradiation Standard[b]	J	σJ	MAP[c] System	Mass Discrim	σ Mass Discrim
Samples included in the youngest population																		
33135-01	AH-3C16/4Fb	1	0.00059	0.00197	0.01232	0.32278	3.3874	46.3	0.14897	0.00524	0.0371	0.0013	ACs	1.3780E-04	2.30E-07	1	1.0037	0.0010
33135-02	AH-3C16/4Fb	1	0.00065	0.00048	0.01225	0.33679	2.9003	42.7	0.14360	0.00578	0.0358	0.0014	ACs	1.3780E-04	2.30E-07	1	1.0037	0.0010
33135-03	*AH-3C16/4Fb*	*1*	*0.00021*	*0.00038*	*0.01236*	*0.19608*	*1.7914*	*67.6*	*0.13209*	*0.00432*	*0.0329*	*0.0011*	*ACs*	*1.3780E-04*	*2.30E-07*	*1*	*1.0037*	*0.0010*
33135-04	*AH-3C16/4Fb*	*1*	*0.00058*	*0.00110*	*0.01234*	*0.30633*	*3.3776*	*43.7*	*0.13349*	*0.00456*	*0.0333*	*0.0011*	*ACs*	*1.3780E-04*	*2.30E-07*	*1*	*1.0037*	*0.0010*
33135-05	AH-3C16/4Fb	1	0.00053	0.00109	0.01222	0.30150	3.3569	47.8	0.14381	0.00497	0.0358	0.0012	ACs	1.3780E-04	2.30E-07	1	1.0037	0.0010
33135-06	AH-3C16/4Fb	1	0.00041	0.00039	0.01204	0.26551	2.5637	53.8	0.14238	0.00450	0.0355	0.0011	ACs	1.3780E-04	2.30E-07	1	1.0037	0.0010
						Weighted Mean (4)			0.14452	0.00253	0.0359	0.0006						
11375-01	AH-18C2	2	0.00011	0.00034	0.01226	0.17822	9.1477	81.8	0.14527	0.00097	0.0358	0.0002	ACs	1.3620E-04	2.00E-07	7	1.0084	0.0016
11375-02	AH-18C2	2	0.00008	0.00027	0.01170	0.17092	7.9215	86.6	0.14747	0.00105	0.0363	0.0003	ACs	1.3620E-04	2.00E-07	7	1.0084	0.0016
11375-03	AH-18C2	2	0.00012	0.00076	0.01218	0.18244	10.9422	81.1	0.14745	0.00110	0.0363	0.0003	ACs	1.3620E-04	2.00E-07	7	1.0084	0.0016
11375-04	AH-18C2	2	0.00041	0.00053	0.01194	0.26514	13.4946	54.6	0.14437	0.00173	0.0356	0.0004	ACs	1.3620E-04	2.00E-07	7	1.0084	0.0016
11375-05	AH-18C2	2	0.00010	0.00034	0.01215	0.17629	8.5324	82.6	0.14501	0.00112	0.0357	0.0003	ACs	1.3620E-04	2.00E-07	7	1.0084	0.0016
11383-01	AH-18C2	2	0.00033	0.00039	0.01209	0.25188	6.8622	60.6	0.15226	0.00208	0.0375	0.0005	ACs	1.3620E-04	2.00E-07	7	1.0084	0.0016
11383-02	AH-18C2	2	0.00023	0.00064	0.01236	0.21886	5.5115	68.4	0.14913	0.00218	0.0367	0.0005	ACs	1.3620E-04	2.00E-07	7	1.0084	0.0016
11383-03	*AH-18C2*	*2*	*0.00044*	*0.00008*	*0.01222*	*1.03607*	*34.0667*	*87.3*	*0.90402*	*0.00345*	*0.2226*	*0.0009*	*ACs*	*1.3620E-04*	*2.00E-07*	*7*	*1.0084*	*0.0016*
11383-04	AH-18C2	2	0.00089	0.00173	0.01208	0.42139	7.2053	37.3	0.15706	0.00510	0.0387	0.0013	ACs	1.3620E-04	2.00E-07	7	1.0084	0.0016
11383-05	*AH-18C2*	*2*	*0.00039*	*-0.00014*	*0.01224*	*0.27807*	*4.4254*	*58.3*	*0.16169*	*0.00313*	*0.0398*	*0.0008*	*ACs*	*1.3620E-04*	*2.00E-07*	*7*	*1.0084*	*0.0016*
11383-06	*AH-18C2*	*2*	*0.00022*	*0.00116*	*0.01231*	*0.21809*	*6.6650*	*69.8*	*0.15181*	*0.00170*	*0.0374*	*0.0004*	*ACs*	*1.3620E-04*	*2.00E-07*	*7*	*1.0084*	*0.0016*
11383-07	*AH-18C2*	*2*	*0.00028*	*-0.00006*	*0.01228*	*0.26652*	*2.7189*	*68.5*	*0.18206*	*0.00447*	*0.0448*	*0.0011*	*ACs*	*1.3620E-04*	*2.00E-07*	*7*	*1.0084*	*0.0016*
						Weighted Mean (8)			0.14646	0.00049	0.0360	0.0001						
11075-01	MAM-01	8	0.00031	0.00108	0.01162	0.25778	3.1643	64.1	0.16466	0.01618	0.0406	0.0040	FCs	1.3630E-04	1.11E-06	7	1.0072	0.0013
11075-02	MAM-01	8	0.00175	0.16989	0.01189	0.68569	9.1936	26.4	0.18061	0.01500	0.0445	0.0037	FCs	1.3630E-04	1.11E-06	7	1.0072	0.0013
11075-03	MAM-01	8	0.00008	0.00021	0.01192	0.16097	3.0096	84.6	0.13554	0.00983	0.0334	0.0024	FCs	1.3630E-04	1.11E-06	7	1.0072	0.0013
11075-04	MAM-01	8	0.00028	0.00101	0.01262	0.21568	3.6699	61.1	0.13139	0.01002	0.0324	0.0025	FCs	1.3630E-04	1.11E-06	7	1.0072	0.0013
11075-05	MAM-01	8	0.00115	0.15910	0.01228	0.47787	5.0531	31.5	0.15010	0.01793	0.0370	0.0044	FCs	1.3630E-04	1.11E-06	7	1.0072	0.0013
11075-06	MAM-01	8	0.00134	0.13060	0.01267	0.52761	8.2898	26.5	0.13982	0.01493	0.0345	0.0037	FCs	1.3630E-04	1.11E-06	7	1.0072	0.0013
11075-07	MAM-01	8	0.00068	0.15759	0.01180	0.34992	5.2010	45.6	0.15910	0.01231	0.0392	0.0031	FCs	1.3630E-04	1.11E-06	7	1.0072	0.0013
11075-08	MAM-01	8	0.00014	0.00089	0.01225	0.16946	1.4144	75.8	0.12798	0.01567	0.0315	0.0039	FCs	1.3630E-04	1.11E-06	7	1.0072	0.0013
						Weighted Mean (8)			0.14535	0.00462	0.0357	0.0011						
33805-01	*AH-17C3*	*1*	*0.00029*	*0.02052*	*0.01205*	*0.27579*	*7.0690*	*69.5*	*0.19114*	*0.00362*	*0.0463*	*0.0009*	*ACs*	*1.3400E-04*	*2.30E-07*	*1*	*1.0120*	*0.0014*
33805-02	AH-17C3	1	0.00022	0.00427	0.01205	0.21735	3.0163	70.8	0.15338	0.00543	0.0372	0.0013	ACs	1.3400E-04	2.30E-07	1	1.0120	0.0014
33805-03	AH-17C3	1	0.00343	0.01222	0.01283	1.14807	9.4371	11.7	0.13408	0.01535	0.0325	0.0037	ACs	1.3400E-04	2.30E-07	1	1.0120	0.0014
33805-04	AH-17C3	1	0.00019	0.00408	0.01223	0.20366	9.2553	72.0	0.14610	0.00209	0.0354	0.0005	ACs	1.3400E-04	2.30E-07	1	1.0120	0.0014
33805-05	*AH-17C3*	*1*	*0.00016*	*0.00442*	*0.01219*	*0.20757*	*4.9211*	*77.7*	*0.16078*	*0.00348*	*0.0390*	*0.0008*	*ACs*	*1.3400E-04*	*2.30E-07*	*1*	*1.0120*	*0.0014*
33805-06	AH-17C3	1	0.00020	0.00397	0.01208	0.21524	2.8759	72.3	0.15521	0.00597	0.0376	0.0014	ACs	1.3400E-04	2.30E-07	1	1.0120	0.0014
33805-07	AH-17C3	1	0.00012	0.00570	0.01225	0.18134	2.1722	80.5	0.14544	0.00545	0.0352	0.0013	ACs	1.3400E-04	2.30E-07	1	1.0120	0.0014
33805-08	*AH-17C3*	*1*	*0.00010*	*0.00731*	*0.01210*	*0.18708*	*6.2241*	*84.1*	*0.15679*	*0.00245*	*0.0380*	*0.0006*	*ACs*	*1.3400E-04*	*2.30E-07*	*1*	*1.0120*	*0.0014*
33805-09	AH-17C3	1	0.00011	0.00365	0.01224	0.18547	2.6690	83.2	0.15370	0.00483	0.0372	0.0012	ACs	1.3400E-04	2.30E-07	1	1.0120	0.0014
33805-10	*AH-17C3*	*1*	*0.00014*	*0.00682*	*0.01208*	*0.19997*	*6.7797*	*79.4*	*0.15827*	*0.00241*	*0.0384*	*0.0006*	*ACs*	*1.3400E-04*	*2.30E-07*	*1*	*1.0120*	*0.0014*
33805-11	AH-17C3	1	0.00015	0.00710	0.01215	0.18740	3.7172	76.9	0.14360	0.00378	0.0348	0.0009	ACs	1.3400E-04	2.30E-07	1	1.0120	0.0014
33805-12	*AH-17C3*	*1*	*0.00015*	*0.00595*	*0.01285*	*0.24371*	*2.5888*	*82.0*	*0.19927*	*0.00661*	*0.0483*	*0.0016*	*ACs*	*1.3400E-04*	*2.30E-07*	*1*	*1.0120*	*0.0014*
33805-13	AH-17C3	1	0.00016	0.00405	0.01211	0.19592	4.3265	76.6	0.14948	0.00377	0.0362	0.0009	ACs	1.3400E-04	2.30E-07	1	1.0120	0.0014
33805-14	*AH-17C3*	*1*	*0.00018*	*0.01622*	*0.01211*	*0.22085*	*6.1969*	*76.9*	*0.16935*	*0.00295*	*0.0410*	*0.0007*	*ACs*	*1.3400E-04*	*2.30E-07*	*1*	*1.0120*	*0.0014*
33805-15	AH17-C3	1	0.00027	0.02417	0.01212	0.22031	4.1813	64.4	0.14140	0.00826	0.0343	0.0020	ACs	1.3400E-04	2.30E-07	1	1.0120	0.0014
33805-16	*AH-17C3*	*1*	*0.00023*	*0.00649*	*0.01255*	*0.27932*	*3.6111*	*75.8*	*0.21128*	*0.00614*	*0.0512*	*0.0015*	*ACs*	*1.3400E-04*	*2.30E-07*	*1*	*1.0120*	*0.0014*
33805-17	AH-17C3	1	0.00008	0.00508	0.01208	0.17863	3.6616	86.6	0.15411	0.00359	0.0373	0.0009	ACs	1.3400E-04	2.30E-07	1	1.0120	0.0014
33805-18	AH-17C3	*1*	0.00007	0.01433	0.01226	0.18570	1.7529	88.7	0.16417	0.00705	0.0398	0.0017	ACs	1.3400E-04	2.30E-07	1	1.0120	0.0014
33805-19	AH-17C3	1	0.00017	0.00484	0.01220	0.20221	3.4363	75.5	0.15207	0.00439	0.0368	0.0011	ACs	1.3400E-04	2.30E-07	1	1.0120	0.0014
33805-20	*AH-17C3*	*1*	*0.00025*	*0.00995*	*0.01211*	*0.24838*	*11.8956*	*70.0*	*0.17346*	*0.00224*	*0.0420*	*0.0005*	*ACs*	*1.3400E-04*	*2.30E-07*	*1*	*1.0120*	*0.0014*
						Weighted Mean (12)			0.14913	0.00122	0.0361	0.0003						

Lab. No	Sample ID	# of crystals	$^{36}Ar/^{39}Ar$	$^{37}Ar/^{39}Ar$	$^{38}Ar/^{39}Ar$	$^{40}Ar/^{39}Ar$	^{40}Ar moles x10^{-15}	$\%^{40}Ar^{*a}$	$^{40}Ar^{*a}/^{39}Ar$	$s\ ^{40}Ar^{*a}/^{39}Ar$	Age (Ma)	$\pm1\sigma^{d}$	Irradiation Standard[b]	J	σJ	MAP[c] System	Mass Discrim	σ Mass Discrim
Samples included in the second youngest population																		
11391-01	*AH-19C1b*	*1*	*0.00034*	*0.00002*	*0.01204*	*1.31293*	*73.6975*	*92.4*	*1.21229*	*0.00296*	*0.2986*	*0.0009*	*ACs*	*1.3620E-04*	*2.00E-07*	*7*	*1.0084*	*0.0016*
11391-02	*AH-19C1b*	*1*	*0.00010*	*-0.00008*	*0.01202*	*1.31841*	*66.6922*	*97.7*	*1.28713*	*0.00262*	*0.3170*	*0.0008*	*ACs*	*1.3620E-04*	*2.00E-07*	*7*	*1.0084*	*0.0016*
11391-03	*AH-19C1b*	*1*	*0.00047*	*-0.00020*	*0.01216*	*1.57331*	*88.5126*	*91.2*	*1.43469*	*0.00373*	*0.3533*	*0.0011*	*ACs*	*1.3620E-04*	*2.00E-07*	*7*	*1.0084*	*0.0016*
11391-04	AH-19C1b	1	0.00013	0.00015	0.01231	0.19822	3.6450	80.1	0.15827	0.00244	0.0390	0.0006	ACs	1.3620E-04	2.00E-07	7	1.0084	0.0016
11391-05	AH-19C1b	1	0.00002	-0.00010	0.01213	0.15986	2.8593	97.2	0.15473	0.00140	0.0381	0.0003	ACs	1.3620E-04	2.00E-07	7	1.0084	0.0016
11391-07	*AH-19C1b*	*1*	*0.00177*	*0.00009*	*0.01249*	*1.98369*	*241.7941*	*73.6*	*1.45951*	*0.00469*	*0.3594*	*0.0013*	*ACs*	*1.3620E-04*	*2.00E-07*	*1*	*1.0037*	*0.0010*
						Weighted Mean[b]			0.15560	0.00122	0.0382	0.0003						
11374-01	*AH-19C2*	*2*	*0.00024*	*0.00121*	*0.01218*	*0.23561*	*10.8236*	*69.4*	*0.16311*	*0.00144*	*0.0402*	*0.0004*	*ACs*	*1.3620E-04*	*2.00E-07*	*7*	*1.0084*	*0.0016*
11374-02	AH-19C2	2	0.00009	0.00047	0.01205	0.18253	7.7204	84.9	0.15436	0.00118	0.0380	0.0003	ACs	1.3620E-04	2.00E-07	7	1.0084	0.0016
11374-03	AH-19C2	2	0.00013	-0.00003	0.01198	0.19950	4.9163	81.0	0.16109	0.00197	0.0397	0.0005	ACs	1.3620E-04	2.00E-07	7	1.0084	0.0016
11374-04	AH-19C2	2	0.00089	0.00226	0.01219	0.42954	18.0279	38.3	0.16430	0.00277	0.0405	0.0007	ACs	1.3620E-04	2.00E-07	7	1.0084	0.0016
11374-05	AH-19C2	2	0.00097	0.00250	0.01256	0.44921	10.5838	36.4	0.16318	0.00258	0.0402	0.0006	ACs	1.3620E-04	2.00E-07	7	1.0084	0.0016
11374-06	AH-19C2	3	0.00007	0.00047	0.01223	0.17883	6.0328	88.9	0.15828	0.00136	0.0390	0.0003	ACs	1.3620E-04	2.00E-07	7	1.0084	0.0016
						Weighted Mean (5)			0.15795	0.00075	0.0388	0.0002						
11376-01	AH-18C3	3	0.00108	0.00172	0.01223	0.47951	26.8060	33.0	0.15811	0.00295	0.0389	0.0007	ACs	1.3620E-04	2.00E-07	7	1.0084	0.0016
11376-02	AH-18C3	3	0.00023	0.00023	0.01203	0.22302	6.5282	69.5	0.15454	0.00186	0.0381	0.0005	ACs	1.3620E-04	2.00E-07	7	1.0084	0.0016
11376-03	*AH-18C3*	*3*	*0.00020*	*0.00304*	*0.01214*	*0.23778*	*11.0015*	*75.6*	*0.17914*	*0.00126*	*0.0441*	*0.0003*	*ACs*	*1.3620E-04*	*2.00E-07*	*7*	*1.0084*	*0.0016*
11376-04	*AH-18C3*	*3*	*0.00057*	*0.00128*	*0.01203*	*0.32383*	*12.3926*	*48.1*	*0.15551*	*0.00206*	*0.0383*	*0.0005*	*ACs*	*1.3620E-04*	*2.00E-07*	*7*	*1.0084*	*0.0016*
11376-05	AH-18C3	3	0.00025	0.00325	0.01224	0.23518	7.0866	69.0	0.16190	0.00193	0.0399	0.0005	ACs	1.3620E-04	2.00E-07	7	1.0084	0.0016
11376-06	AH-18C3	3	0.00036	0.00081	0.01189	0.26891	7.8165	59.8	0.16043	0.00215	0.0395	0.0005	ACs	1.3620E-04	2.00E-07	7	1.0084	0.0016
						Weighted Mean (4)			0.15866	0.00106	0.0390	0.0003						
33136-01	AH-3C14	1	0.00073	0.00292	0.01190	0.37697	3.3865	42.3	0.15906	0.00687	0.0396	0.0017	ACs	1.3780E-04	2.30E-07	1	1.0060	0.0022
33136-02	AH-3C14	2	0.00257	0.00085	0.01277	0.91718	8.0627	17.1	0.15716	0.01190	0.0392	0.0030	ACs	1.3780E-04	2.30E-07	1	1.0060	0.0022
33136-03	AH-3C14	5	0.00154	0.01835	0.01288	0.63371	5.6328	28.0	0.17725	0.00857	0.0442	0.0021	ACs	1.3780E-04	2.30E-07	1	1.0060	0.0022
33136-04	AH-3C14	3	0.00029	0.00056	0.01177	0.24787	2.3042	65.7	0.16249	0.00476	0.0405	0.0012	ACs	1.3780E-04	2.30E-07	1	1.0060	0.0022
33136-05	*AH-3C14*	*4*	*0.00099*	*0.00046*	*0.01215*	*0.48203*	*2.8308*	*39.4*	*0.18963*	*0.00909*	*0.0473*	*0.0023*	*ACs*	*1.3780E-04*	*2.30E-07*	*1*	*1.0060*	*0.0022*
33136-06	AH-3C14	3	0.00077	0.00757	0.01236	0.39786	2.6948	42.5	0.16892	0.00782	0.0421	0.0020	ACs	1.3780E-04	2.30E-07	1	1.0060	0.0022
						Weighted Mean (5)			0.16440	0.00312	0.0409	0.0008						
11348-01	AH-9	1	0.00026	0.00000	0.01199	0.24411	5.6668	67.9	0.16533	0.01270	0.0383	0.0029	ACs	1.2800E-04	2.00E-07	2	1.0070	0.0020
11348-02	AH-9	1	0.00055	0.00000	0.01229	0.34362	8.1535	52.8	0.18106	0.01268	0.0419	0.0029	ACs	1.2800E-04	2.00E-07	2	1.0070	0.0020
11348-03	AH-9	1	0.00057	0.00000	0.01216	0.34163	6.2465	50.7	0.17295	0.01621	0.0400	0.0038	ACs	1.2800E-04	2.00E-07	2	1.0070	0.0020
11348-04	AH-9	2	0.00056	0.00000	0.01210	0.35004	12.9988	52.1	0.18194	0.00878	0.0421	0.0020	ACs	1.2800E-04	2.00E-07	2	1.0070	0.0020
11348-05	AH-9	2	0.00038	0.00000	0.01200	0.29319	10.6330	61.2	0.17913	0.00836	0.0415	0.0019	ACs	1.2800E-04	2.00E-07	2	1.0070	0.0020
11348-06	AH-9	2	0.00056	0.00000	0.01201	0.34582	10.3259	51.8	0.17869	0.01029	0.0414	0.0024	ACs	1.2800E-04	2.00E-07	2	1.0070	0.0020
						Weighted Mean (6)			0.17791	0.00435	0.0411	0.0010						
33132-01	AH-3C12L	1	0.00342	0.00126	0.01278	1.17263	13.6172	13.6	0.15952	0.01587	0.0397	0.0040	ACs	1.3780E-04	2.30E-07	1	1.0060	0.0022
33132-02	*AH-3C12L*	*1*	*0.00023*	*0.00004*	*0.01175*	*0.24191*	*1.9022*	*71.7*	*0.17291*	*0.00511*	*0.0431*	*0.0013*	*ACs*	*1.3780E-04*	*2.30E-07*	*1*	*1.0060*	*0.0022*
33132-03	*AH-3C12L*	*1*	*0.00114*	*0.00004*	*0.01240*	*1.77280*	*15.2073*	*80.9*	*1.43329*	*0.00897*	*0.3571*	*0.0023*	*ACs*	*1.3780E-04*	*2.30E-07*	*1*	*1.0060*	*0.0022*
33132-04	AH-3C12L	1	0.00041	0.00010	0.01219	0.28229	1.7970	56.7	0.15955	0.00637	0.0398	0.0016	ACs	1.3780E-04	2.30E-07	1	1.0060	0.0022
33132-05	AH-3C12L	1	0.00138	0.00034	0.01239	0.58561	6.1863	30.0	0.17550	0.00737	0.0437	0.0018	ACs	1.3780E-04	2.30E-07	1	1.0060	0.0022
33132-06	*AH-3C12L*	*1*	*0.00215*	*0.00088*	*0.01276*	*0.83771*	*9.9572*	*23.9*	*0.19990*	*0.00944*	*0.0498*	*0.0024*	*ACs*	*1.3780E-04*	*2.30E-07*	*1*	*1.0060*	*0.0022*
33132-07	*AH-3C12L*	*1*	*0.00031*	*0.00043*	*0.01249*	*0.26831*	*3.3822*	*65.2*	*0.17450*	*0.00384*	*0.0435*	*0.0010*	*ACs*	*1.3780E-04*	*2.30E-07*	*1*	*1.0060*	*0.0022*
33132-08	*AH-3C12L*	*1*	*0.00064*	*0.00150*	*0.01214*	*0.41795*	*3.4721*	*54.6*	*0.22797*	*0.00591*	*0.0568*	*0.0015*	*ACs*	*1.3780E-04*	*2.30E-07*	*1*	*1.0060*	*0.0022*
						Weighted Mean[c]			0.16580	0.00461	0.0412	0.0011						
33131-01	AH-3C12S	*1*	0.00491	0.01666	0.01294	1.63911	6.0013	11.3	0.18497	0.01671	0.0461	0.0042	ACs	1.3780E-04	2.30E-07	1	1.0060	0.0022
33131-02	*AH-3C12S*	*2*	0.00375	0.00574	0.01265	1.29326	5.0506	14.1	0.18248	0.01378	0.0455	0.0034	ACs	1.3780E-04	2.30E-07	1	1.0060	0.0022
33131-03	*AH-3C12S*	*2*	*0.00082*	*0.04261*	*0.01271*	*0.43268*	*1.3063*	*44.8*	*0.19336*	*0.01376*	*0.0482*	*0.0034*	*ACs*	*1.3780E-04*	*2.30E-07*	*1*	*1.0060*	*0.0022*
33131-04	*AH-3C12S*	*2*	*0.00099*	*0.00870*	*0.01236*	*2.05378*	*8.0654*	*85.7*	*1.76019*	*0.01354*	*0.4386*	*0.0035*	*ACs*	*1.3780E-04*	*2.30E-07*	*1*	*1.0060*	*0.0022*
33131-05	*AH-3C12S*	*2*	*0.01002*	*0.01015*	*0.01384*	*6.21012*	*22.4909*	*52.2*	*3.24375*	*0.04212*	*0.8081*	*0.0106*	*ACs*	*1.3780E-04*	*2.30E-07*	*1*	*1.0060*	*0.0022*

Lab. No	Sample ID	# of crystals	$^{36}Ar/^{39}Ar$	$^{37}Ar/^{39}Ar$	$^{38}Ar/^{39}Ar$	$^{40}Ar/^{39}Ar$	^{40}Ar moles $x10^{-15}$	$\%^{40}Ar^{*a}$	$^{40}Ar^{*a}/^{39}Ar$	$s\ ^{40}Ar^{*a}/^{39}Ar$	Age (Ma)	$\pm1\sigma^{d}$	Irradiation Standard[b]	J	σJ	MAP[c] System	Mass Discrim	σ Mass Discrim
33131-06	*AH-3C12S*	2	0.00190	0.06457	0.01257	0.72616	1.0800	23.1	0.16736	0.02623	0.0417	0.0065	ACs	1.3780E-04	2.30E-07	1	1.0060	0.0022
						Weighted Mean[c]			0.18121	0.00985	0.0450	0.0024						
Samples included in the oldest population																		
33137-01	AH-3C9	2	0.00235	0.00347	0.01271	0.96698	7.6018	28.2	0.27232	0.00842	0.0679	0.0021	ACs	1.3780E-04	2.30E-07	1	1.0060	0.0022
33137-02	AH-3C9	3	0.00129	0.00054	0.01237	0.65765	5.7569	41.9	0.27527	0.00814	0.0686	0.0020	ACs	1.3780E-04	2.30E-07	1	1.0060	0.0022
33137-03	AH-3C9	4	0.00231	0.00290	0.01249	0.97249	7.7320	29.7	0.28872	0.00813	0.0719	0.0020	ACs	1.3780E-04	2.30E-07	1	1.0060	0.0022
33137-04	AH-3C9	3	0.01645	0.58135	0.01509	5.03753	23.7445	4.3	0.21434	0.04982	0.0534	0.0124	ACs	1.3780E-04	2.30E-07	1	1.0060	0.0022
33137-05	AH-3C9	5	0.00943	0.18034	0.01427	3.05450	32.7308	9.1	0.27650	0.02893	0.0689	0.0072	ACs	1.3780E-04	2.30E-07	1	1.0060	0.0022
33137-06	AH-3C9	4	0.00418	0.06156	0.01297	1.48633	15.1976	17.0	0.25258	0.01415	0.0629	0.0035	ACs	1.3780E-04	2.30E-07	1	1.0060	0.0022
						Weighted Mean (6)			0.27577	0.00443	0.0686	0.0011						
11385-01	AH-18C1	2	0.00117	0.00197	0.01236	0.62952	30.3532	45.0	0.28288	0.00348	0.0697	0.0009	ACs	1.3620E-04	2.00E-07	7	1.0084	0.0016
11385-02	*AH-18C1*	*2*	*0.00020*	*0.00009*	*0.01212*	*0.34753*	*14.6556*	*82.7*	*0.28692*	*0.00232*	*0.0707*	*0.0006*	*ACs*	*1.3620E-04*	*2.00E-07*	*7*	*1.0084*	*0.0016*
11385-03	AH-18C1	2	0.00018	-0.00003	0.01217	0.33606	9.3218	84.5	0.28343	0.00168	0.0698	0.0004	ACs	1.3620E-04	2.00E-07	7	1.0084	0.0016
11385-04	AH-18C1	2	0.00044	0.00090	0.01222	0.40757	10.5385	68.1	0.27709	0.00219	0.0682	0.0005	ACs	1.3620E-04	2.00E-07	7	1.0084	0.0016
11385-05	AH-18C1	1	0.00026	0.00016	0.01206	0.35760	23.4053	78.3	0.27952	0.00138	0.0688	0.0004	ACs	1.3620E-04	2.00E-07	7	1.0084	0.0016
						Weighted Mean (4)			0.28050	0.00092	0.0689	0.0002						
11334-01	AH-3A	1	0.00030	0.00000	0.01210	0.38951	30.7916	77.3	0.30063	0.00506	0.0702	0.0012	ACs	1.2920E-04	2.00E-07	2	1.0070	0.0020
11334-02	AH-3A	1	0.00059	0.00000	0.01222	0.47187	43.1380	62.7	0.29528	0.00496	0.0690	0.0012	ACs	1.2920E-04	2.00E-07	2	1.0070	0.0020
11334-03	AH-3A	1	0.00182	0.00000	0.01251	0.82980	46.8417	34.9	0.28915	0.00841	0.0676	0.0020	ACs	1.2920E-04	2.00E-07	2	1.0070	0.0020
11334-04	AH-3A	1	0.00026	0.00000	0.01162	0.36915	17.4903	78.8	0.29026	0.00710	0.0678	0.0017	ACs	1.2920E-04	2.00E-07	2	1.0070	0.0020
11334-05	AH-3A	1	0.00080	0.00000	0.01228	0.54575	36.6348	56.6	0.30842	0.00655	0.0721	0.0015	ACs	1.2920E-04	2.00E-07	2	1.0070	0.0020
						Weighted Mean (5)			0.29768	0.00270	0.0694	0.0006						

Notes:

Samples in italics were interpeted to be xenocrysts and/or were eliminated to reduce the MSWD to below 1.5 (see text for explanation)

These data were eliminated from the error-weighted mean calculations for each sample above, and were eliminated from the ideogram and isochron plots in the paper

[a]$^{40}Ar^{*}$ = radiogenic ^{40}Ar

[b]Irradiation standards: Alder Creek rhyolite sanidine (ACs, 1.19 Ma, Renne et al. 1998) or Fish Canyon tuff sanidine (FCs, 28.02 Ma, Renne et al. 1998)

[c]MAP = Mass Analyzer Products spectrometer system at the Berkeley Geochronology Center. For further information on this system please refers to BGC's website (http://www.bgc.org)

Appendix B

Methodology

Geochronological data

$^{40}Ar/^{39}Ar$ analyses were performed at the Berkeley Geochronology Center generally following methods described previously (Karner and Renne 1998). Mineral separates were cleaned in an ultrasonic bath of 7% HF for approximately 60 seconds to remove adhered glass and to reduce surficial atmospheric argon contamination. Leucite separates were placed in aluminum disks along with the Alder Creek rhyolite sanidine mineral standard (ACs, 1.194 Ma, Renne et al. 1998) and irradiated in the CLICIT facility at the Oregon State University TRIGA reactor for approximately 30 min, where cadmium shielding is employed to minimize the $^{40}K(n,p)$ ^{40}Ar reaction caused by thermal neutrons (Tetley et al. 1980). Decay constants and isotopic abundances of potassium are those recommended by Steiger and Jaeger (1977) with uncertainties reported by McDougall and Harrison (1988).

Two fully automated microextraction-mass spectrometer systems were used for the $^{40}Ar/^{39}Ar$ analyses, as described by Karner and Renne (1998). The MAP1 system includes a 6 W continuous Ar-ion laser for sample heating, and a Mass Analyzer Products (MAP) 215 90° sector extended-geometry mass spectrometer for isotopic analysis. MAP-III includes a CO_2 laser, and a MAP 215-50 90° sector extended-geometry mass spectrometer with electrostatic analyzer. Background corrections were made from full system blanks, which were run between every three unknowns. Released gases were scrubbed of reactive species using Zr-Fe-V and Zr-Al alloy getters, and the remaining gases were then admitted into the mass spectrometer, where the Ar ion beam currents were measured on an electron multiplier. Mass discriminations (1.0088±0.0016/amu for MAP1, 1.0084±0.0038/amu for MAPIII), applied as a power law correction were determined by analysis of atmospheric argon from air pipettes. Argon isotopes were corrected using procedural blanks; long-term blank values were regressed such that between-blank variance was propagated as a component of uncertainty.

Major and trace elements analyses

Major element analyses of the various phases were performed at the CNR-Istituto di Geologia Ambientale e Geoingegneria (Rome, Italy) with a Cameca SX50 electron microprobe equipped with five wavelength-dispersive spectrometers using 15 kV accelerating voltage, 15 nA beam current, 10 μm beam diameter, and 20 s counting time. The following standards were used: wollastonite (Si and Ca), corundum (Al), diopside (Mg), andradite (Fe), rutile (Ti), orthoclase (K), jadeite (Na), barite (Ba), celestine (Sr), F-phlogopite (F), baritine (S), and metals (Cr and Mn). Ti and Ba contents were corrected for the overlap of the Ti K_α and Ba K_α peaks. The verified lack of correlation between elements not detectable using the electron microprobe (e.g. H_2O and CO_2, see Devine et al. 1995) and Na_2O or F, indicates that the loss of light elements was minimized and justify the use of Na_2O content as differentiation index.

Trace elements in clinopyroxenes were measured by the laser probe installed at the CNR-IGG-Pavia couples a pulsed Nd:YAG laser source working at 213 nm with an ICP sector field mass spectrometer Element I (ThermoFinnigan). Instrumental and analytical details are reported in Tiepolo et al. (2003). For the present work, the laser was operated at a repetition rate of 10 Hz, and the spot diameter was set at 45 μm with a pulse energy of about 0.1 mJ. Ablation signal integration intervals have been selected by carefully inspecting the time-resolved analysis to ensure that no inclusions were present in the analyzed volume. Data reduction was performed by the software package "Glitter" (van Achterbergh et al. 1999). NIST SRM 612 was used as the external standard, whereas ^{44}Ca was used as internal standard. Reproducibility and accuracy of the REE concentration values were assessed on the control sample BCR2-g (MUN, ICP-MS unpublished data) to be $<7\%$ and $<10\%$ relative, respectively.

$\delta^{18}O$ values determination

The stable isotope were measured by laser fluorination (Sharp 1992) at the CNR-Istituto di Geologia Ambientale e Geoingegneria (Rome, Italy). In order to measure the oxygen isotope composition of each phase, 1 to 1.5 mg aliquots of unaltered and inclusion-free mineral separate are taken and laser fluorinated. A 15 Watts CO_2 laser, operating at a wavelength of 10.6 μm is used to irradiate the samples placed in a 3 mm diameter hole, within a 32-hole nickel sample plug. Pure fluorine desorbed at 290–310 °C from hexafluoropotassium-nickelate salt (Asprey 1976) and stored in a F_2 reservoir, are used as reagent. The O_2 produced during laser fluorination is purified from excess fluorine by means of a KBr trap held at 180 °C, and the bromine trapped cryogenically. The gas is then transferred to a 13 Å molecular sieve-filled cold finger. Further oxygen gas purification is achieved desorbing oxygen from the molecular sieve at about −110 °C, using a liquid nitrogen-ethanol mixture. In this way the NF compounds are retained on the 13 Å zeolites (Clayton and Mayeda 1983). The gas is then analyzed for oxygen isotope composition using a Finnigan Delta Plus Mass Spectrometer. On each day of analysis, four to seven aliquots of our laboratory quartz standards are normally analyzed, with an average reproducibility of ±0.12‰ (1σ). No data correction is necessary for the results, which are reported in the standard per mil notation. All $\delta^{18}O$ values are relative to SMOW.

$^{87}Sr/^{86}Sr$ ratio determination

$^{87}Sr/^{86}Sr$ ratios were determined at the Center for Isotope Geochemistry, Lawrence Berkeley National Laboratory

(Berkeley, USA). Clinopyroxene for Sr isotopic analyses were hand picked into separates, where appropriate, of dark and light (or in some cases zoned) crystals. Before dissolution, the clinopyroxene samples were cleaned in dilute HF and HCl (approximately 5% each) for 10 min in an ultrasonic cleaner. The acid solution was then decanted with a pipette, and the separate repeatedly rinsed with super DI water. The separates were then dried, weighed out, and dissolved in closed Savilex Teflon vials with a mixture of concentrated HNO_3 and HF on a hotplate. The samples were then dried down and taken up in concentrated HNO_3 and several drops of $HClO_4$ and dried down once again. For Sr separation, the samples were taken up in 3N HNO_3 and loaded on small columns of Sr specific resin (EiChrom Inc.). The sample Sr was eluted with DI water, dried down with a drop of $HClO_4$ in preparation for loading with tantalum chloride solution on an outgassed Re filament for thermal ionization mass spectrometric analysis. Samples were analyzed for Sr isotopic composition on a VG 54 multicollector mass spectrometer using a multidynamic analysis routine, with normalization to $^{86}Sr/^{88}Sr = 0.1194$.

References

Asprey LB (1976) The preparation of very pure F2 gas. J Fluorine Chem 7:359–361

Bohrson WA, Spera FJ (2001) Energy-constrained open-system magmatic processes II: application of Energy-Constrained Assimilation-Fractional Crystallization (EC-AFC) model to magmatic system. J Petrol 42:1019–1041

Caputo C, Ciccacci S, D'Alessandro L, Davoli L, Fredi P, La Monica GB, Lupia Palmieri E, Pugliese F, Raffi R (1986) Progetto "Lago Albano". Indagini climatiche, geomorfologiche e sedimentologiche. Ed. by Provincia di Roma, Rome, Italy, pp 1–14

Civitelli G, Funiciello R, Parotto M (1975) Caratteri deposizionali dei prodotti del vulcanismo freatico dei Colli Albani. Geologica Romana 14:1–39

Clayton RN, Mayeda TK (1983) Oxygen isotopes in eucrites, shergottites, nakhilites, and chassignites. Earth Planet Sci Lett 62:1–6

Conticelli S, D'Antonio M, Pinarelli L, Civetta L (2002) Source contamination and mantle heterogeneity in the genesis of Italian potassic and ultrapotassic volcanic rocks: Sr-Nd-Pb isotope data from Roman Province and Southern Tuscany. Mineral Petrol 74:189–222

Conticelli S, Peccerillo A (1992) Petrology and geochemistry of potassic and ultrapotassic volcanism in central Italy: petrogenesis and inferences on the evolution of the mantle sources. Lithos 28:221–240

Dallai L, Freda C, Gaeta M (2004) Oxygen isotope geochemistry of pyroclastic clinopyroxene monitors carbonate contributions to Roman-type ultrapotassic magmas. Contrib Mineral Petrol DOI 10.1007/s00410-004-0602-2

De Paolo DJ (1981) Trace element and isotopic effects of combined wall-rock assimilation and fractional crystallization. Earth Planet Sci Lett 53:189–202

De Rita D, Faccenna C, Funiciello R, Rosa C (1995a) Stratigraphy and volcano-tectonics. In: Trigila R (ed) The volcano of the Alban Hills. Università degli Studi di Roma "La Sapienza", Rome, Italy, pp 33–71

De Rita D, Giordano G, Rosa C, Sheridan MF (1995b) Volcanic hazard at the Alban Hills and computer simulations. In: Trigila R (ed) The volcano of the Alban Hills. Università degli Studi di Roma "La Sapienza", Rome, Italy, pp 267–283

De Rita D, Funiciello R, Parotto M (1988) Carta geologica del Complesso vulcanico dei Colli Albani, Progetto Finalizzato 'Geodinamica', C.N.R., Rome, Italy

Devine JD, Gardner JE, Brack HP, Layne GD, Rutherford MJ (1995) Comparison of microanalytical methods for estimating H_2O content in silicic glasses. Am Mineral 80:319–328

Di Battistini G, Montanini A, Vernia L, Bargossi GM, Castorina F (1998) Petrology and geochemistry of ultrapotassic rocks from the Montefiascone Volcanic complex (Central Italy): magmatic evolution and petrogenesis. Lithos 43:169–195

Doglioni C, Harabaglia P, Merlini S, Mongelli F, Peccerillo A, Piromallo C (1999) Orogens and slabs vs. their direction of subduction. Earth Sci Rev 45:167–20

Einaudi MT, Meinert LD, Newberry RJ (1981) Skarn deposits. Econ Geol 75th Anniv, pp 317–391

Federico M, Peccerillo A, (2002) Mineral chemistry and petrogenesis of granular ejecta from the Alban Hills volcano (Central Italy). Mineral Petrol 74:223–252

Federico M, Peccerillo A, Barbieri M, Wu TW (1994) Mineralogical and geochemical study of granular xenoliths from the Alban Hills volcano, Central Italy: bearing on evolutionary processes in potassic magma chambers. Contrib Mineral Petrol 115:384–401

Ferrara G, Laurenzi MA, Taylor HP Jr, Tonarini S, Turi B (1985) Oxygen and strontium isotope studies of K-rich volcanic rocks from the Alban Hills, Italy. Earth Planet Sci Lett 75:13–28

Fisher RV, Schmincke HU (1984) Pyroclastic Rocks. Springer, Berlin Heidelberg New York, 472 pp

Foley SF, Venturelli G, Green DH, Toscani L (1987) The ultrapotassic rocks: characteristics, classification, and constraints for petrogenetic models. Earth Sci Rev 24:81–134

Fornaseri M, Scherillo A, Ventriglia U (1963) La regione vulcanica dei Colli Albani. Consiglio Nazionale delle Ricerche, Rome, 561 pp

Fornaseri M, Cortesi C (1989) Recenti acquisizioni sull'età del "Peperino"di Albano. Docum Albana II, pp. 7–10

Fornaseri M, Turi B (1969) Carbon and oxygen isotopic composition of carbonates in lavas and ejectites from Alban Hills, Italy. Contrib Mineral Petrol 23:244–256

Freda C, Gaeta M, Palladino DM, Trigila R (1997) The Villa Senni Eruption (Alban Hills, central Italy): the role of H_2O and CO_2 on the magma chamber evolution and on the eruptive scenario. J Volcanol Geotherm Res 78A:103–120

Funiciello R, Giordano G, De Rita D (2003) The Albano maar lake (Colli Albani Volcano, Italy): recent volcanic activity and evidence of pre-Roman Age catastrophic lahar events. J Volcanol Geotherm Res 123:43–61

Funiciello R, Giordano G, De Rita D, Carapezza ML, Barberi F (2002) L'attività recente del cratere del Lago di Albano di Castelgandolfo. Rend Acc dei Lincei 13:113–143

Gaeta M (1998) Petrogenetic implications of Ba-sanidine in the Lionato Tuff (Colli Albani Volcanic District, Central Italy). Mineral Mag 62:697–701

Gaeta M, Fabrizio G, Cavarretta G (2000) F-phlogopites in the Alban Hills Volcanic District (Central Italy): Indications regarding the role of volatiles in magmatic crystallization. J Volcanol Geotherm Res 99:179–193

Gaeta M, Freda C (2001) Strontian fluoro-magnesiohastingsite in Alban Hills lavas (Central Italy): crystallization conditions. Mineral Mag 65:717–779

Gaeta M, Freda C, Christensen JN, Dallai L, Marra F, Karner DB, Scarlato P (2005) Evolution of the mantle source region for ultrapotassic magmas of the Alban Hills volcanic district, Central Italy. Lithos doi: 10.1016/j.lithos.2005.05.010

Giordano G, De Rita D, Cas R, Rodani S (2002) Valley pond and ignimbrite veneer deposits in the small-volume phreatomagmatic 'Peperino Albano' basic ignimbrite, Lago Albano maar, Colli Albani volcano, Italy: influence of topography. J Volcanol Geotherm Res 118:131–144

Gittings J (1979) The feldspathoidal alkaline rocks. In: Yoder HS (ed) Evolution of igneous rocks. Princeton University Press, pp 361–390

Gustafson WI (1974) The stability of andradite, hedenbergite, and related minerals in the system Ca-Fe-Si-O-H. J Petrol 15:455–496
Hart SR, Dunn T (1993) Experimental clinopyroxene/melt partitioning of 24 trace elements. Contrib Mineral Petrol 113:1–8
Hermes OD, Cornell WC (1981) Quenched crystal mush and associated magma compositions as indicated by intercumulus glasses from Mt. Vesuvius, Italy. J Volcanol Geotherm Res 9:133–149
Karner DB, Lombardi L, Marra F, Fortini P, Renne PR (2001a) Age of ancient monuments by means of building stone provenance: a case study of the Tullianum, Rome, Italy. J Archaeol Sc 28:387–393
Karner DB, Marra F, Florindo F, Boschi E (2001b) Pulsed uplift around Rome: evidence for a new phase of volcanic activity? Earth Planet Sci Lett 188:135–148
Karner DB, Marra F, Renne P (2001c) The History of the Monti Sabatini and Alban Hills Volcanoes: groundwork for assessing volcanic-tectonic hazards for Rome. J Volcanol Geotherm Res 107:185–219
Karner DB, Renne P (1998) $^{40}Ar/^{39}Ar$ geochronology of Roman Volcanic Province tephra in the River Tiber valley: age calibration of Middle Pleistocene sea-level changes. Geol Soc Am Bull 110:740–747
Marra F, Freda C, Scarlato P, Taddeucci J, Karner DB, Renne P, Gaeta M, Palladino DM, Trigila R, Cavarretta G (2003) $^{40}Ar/^{39}Ar$ Geochronology of the recent phase of activity of the Alban Hills Volcanic District (Rome, Italy): implications for seismic and volcanic hazards. Bull Volcanol 65:227–247
Marra F, Taddeucci J, Freda C, Marzocchi W, Scarlato P (2004) Eruption recurrence interval of the Alban Hills and coupling with other volcanic districts of the Tyrrhenian margin of Italy: possible tectonic influence and implications for volcanic hazard. Tectonics DOI 10.1029/2003TC001600
McDougall I, Harrison TM (1988) Geochronology and thermochronology by the $^{40}Ar/^{39}Ar$ method. Oxford Monographs on Geology and Geophysics, 9. Oxford University Press, 212 p
Morimoto N et al (1988) Nomenclature of pyroxenes. Mineral Mag 52:535–550
Palladino DM, Gaeta M, Marra F (2001) A large K-foiditic hydromagmatic eruption from the early activity of the Alban Hills Volcanic District (Italy). Bull Volcanol 63:345–359
Peccerillo A (1985) Roman Comagmatic Province (Central Italy): evidence for subduction-related magma genesis. Geology 13:103–106
Peccerillo A, Manetti P (1985) The potassium alkaline volcanism of Central-Southern Italy: a review of the data relevant to petrogenesis and geodynamic significance. Trans Geol Soc S Afr 88:379–394
Peccerillo A, Poli G, Tolomeo L (1984) Genesis, evolution and tectonics significance of K-rich volcanics from the Alban Hills (Roman Comagmatic Region) as inferred from trace element geochemistry. Contrib Mineral Petrol 86:230–240
Perini G, Francalanci L, Davidson JP, Ponticelli S (2004) Evolution and genesis of magmas from Vico Volcano, Central Italy: multiple differentiation pathways and variable parental magmas. J Petrol 45:139–182
Renne PR, Deckart K, Ernesto M, Féraud G, Piccirillo EM (1996) Age of the Ponta Grossa Dike Swarm (Brazil) and implications for Paraná flood volcanism. Earth Planet Sci Lett 144:199–211
Renne PR, Swisher CC, Deino AL, Karner DB, Owens T, De Paolo DJ (1998) Intercalibration of standards, absolute ages and uncertainties in $^{40}Ar/^{39}Ar$ dating. Chem Geol 145:117–152
Sharp ZD (1992) In situ laser microprobe techniques for stable isotope analysis. Chem Geol 101:3–19
Soligo M, Tuccimei P, Giordano G, Funiciello R, De Rita D (2003) New U-series dating of a carbonate level underlying the Peperino Albano phreatomagmatic ignimbrite (Colli Albani, Italy). Il Quaternario 16:115–120
Spencer KJ, Lindsley DH (1981) A solution model for coexisting iron-titanium oxides. Am Mineral 66:1189–1201
Steiger RH, Jaeger E (1977) Subcommission on geochronology: convention on the use of decay constants in geo- and cosmochronology. Earth Planet Sci Lett 36:359–362
Sun SS, McDonough WF (1989) Chemical and isotopic systematic of oceanic basalts: implication for mantle composition and processes. In: Saunders AD, Norry MG (eds) Magmatism in ocean basins. Geol Soc Spec Publ 42:313–345
Tetley N, McDougall I, Heydegger HR (1980) Thermal neutron interferences in the $^{40}Ar/^{39}Ar$ dating technique. J Geophys Res 85:7201–7205
Tiepolo M, Bottazzi P, Palenzona M, Vannucci R (2003) A laser probe coupled with ICP-double-focusing sector-field mass spectrometer for in situ analysis of geological samples and U-Pb dating of zircon. Can Mineral 41:259–272
Trigila R, Agosta E, Currado C, De Benedetti AA, Freda C, Gaeta M, Palladino DM, Rosa C (1995) Petrology. In: Trigila R (ed) The volcano of the Alban Hills. Università degli Studi di Roma "La Sapienza", Rome, pp 95–165
Turi B (1970) Carbon and oxygen isotopic composition of carbonates in limestone blocks and related geodes from the "Black Pozzolans" formation of the Alban Hills. Chem Geol 5:195–205
van Achterbergh E, Ryan CG, Griffin WL (1999): GLITTER: on-line interactive data reduction for the laser ablation ICP-MS microprobe. Proc 9th Ann V.M. Goldschmidt Conf, Boston, USA, 7215
Vasconcelos P, Brimhall GH, Becker TA, Renne PR (1994) $^{40}Ar/^{39}Ar$ analysis of supergene jarosite and alunite: Implications to the paleoweathering history of western US and west Africa. Geochim Cosmochim Acta 58:401–420
Villa IM, Calanchi N, Dinelli E, Lucchini F (1999) Age and evolution of the Albano crater lake (Roman Volcanic Province). Acta Vulcanol 11:305–310